

Exploratory Factor Analysis of Data on a Sphere

Fan Dai, Karin S. Dorman, Somak Dutta and and Ranjan Maitra

Data on high-dimensional spheres arise frequently in many disciplines either naturally or as a consequence of preliminary processing and can have intricate dependence structure that needs to be understood. We develop exploratory factor analysis of the projected normal distribution to explain the variability in such data using a few easily interpreted latent factors. Our methodology provides maximum likelihood estimates through a novel fast alternating expectation profile conditional maximization algorithm. Results on simulation experiments on a wide range of settings are uniformly excellent. Our methodology provides interpretable and insightful results when applied to tweets with the #MeToo hashtag in early December 2018, to time-course functional Magnetic Resonance Images of the average pre-teen brain at rest, to characterize handwritten digits, and to gene expression data from cancerous cells in the Cancer Genome Atlas.

Index Terms

AECM, l_2 -normalization, Lanczos algorithm, matrix-free computations, #MeToo, MNIST, projected normal distribution, resting state fMRI, term-document matrix, TCGA.

I. INTRODUCTION

Observations that lie on a unit sphere [1], [2], [3], [4] arise naturally in disciplines such as astronomy (*e.g.*, the orientation of planetary and cometary orbits), biology (*e.g.*, homing behavior or the direction of capillaries in tissue), geology (*e.g.*, the orientation of paleomagnetism in rocks or the axes of sand dunes), meteorology (*e.g.*, wind direction), oceanography (*e.g.*, the direction of ice flows) or physics (*e.g.*, the direction of particle diffusion). Many distributions [3], [4] have been proposed to model such observations, but the von Mises (or circular normal) distribution [5] is commonly used to model angular data, while observations on a three-dimensional sphere are often modeled with the Fisher distribution [6]. The von Mises and Fisher distributions are the 2- and 3-dimensional cases of the Langevin [1] distribution – also called the Fisher-von Mises [7] or von Mises-Fisher [4] distribution – that models data on a multi-dimensional sphere. However, this distribution is unable to adequately characterize relationships between variables, especially in the context of modern applications such as text processing, genetics or imaging, where observations end up on unit spheres after appropriate processing. We describe four motivating applications with high-dimensional data on unit spheres that can benefit from a distribution that can characterize dependence between variables.

A. Motivating Applications

We introduce four scenarios where preprocessing yields unit-sphered data. In each case, the goal is to characterize variability and relationships between variables, whether they are words in tweets containing the hashtag #MeToo, the time-points in temporal functional Magnetic Resonance Imaging (fMRI) data of an averaged typically developing child brain at rest, pixels in bitmap images, or cancerous gene expressions in the Cancer Genome Atlas (TCGA).

1) *Summarizing #MeToo tweets:* The #MeToo hashtag on Twitter provided an online forum for women to narrate their harassment or abuse at the hands of men in positions of authority. The term had been percolating in social media since 2006, but received a major fillip in 2017 with the outing of high-profile abusers in entertainment, politics, business and media. Our interest is in characterizing variability in tweets having the hashtag and to countenance its description by a few underlying factors. Each tweet is akin to a text document, so all the tweets can be processed into a weighted *document-term frequency matrix* [8], [9], [10], with the most common weighting scheme normalizing each tweet to lie on a high-dimensional unit sphere [11]. Modeling each tweet in terms of the Langevin distribution, as commonly done for text data [12], would require marginal exchangeability and essentially no correlation between words and a characterization totally at odds with the reality of tweet structure and characteristics. We return to this dataset in Section IV-A.

2) *Characterizing the brain at rest:* Characterizing changes in cerebral blood-flow at rest [13], or in the absence of any stimulus or task, is of interest to researchers [14]. A typical resting state experiment using fMRI [15], [16], [17], [18], [19] involves collecting a time series of blood-oxygen-level-dependent (BOLD) images of the brain at rest, and after preprocessing, fitting a linear model at each voxel with motion and other structured noise as covariates. The time series of the residuals, or the part of the BOLD response vector unexplained by the linear model, is the resting state component of the dataset [20], [21]. Functionally connected voxels may be detected from correlations between the residual time series sequences at each voxel, or equivalently by calculating the Euclidean distance between the centered and standardized time series that lie on the unit sphere [22]. However, it may also be of interest to characterize the distribution and variability of activity patterns in the resting state brain, for which the Langevin distribution is again inadequate. We revisit this application in Section IV-B.

F. Dai is with the Department of Mathematical Sciences at the Michigan Technological University, Houghton, Michigan 49931, USA. e-mail: fand@mtu.edu.

K.S. Dorman is with the Departments of Statistics and Genetics Development and Cell Biology, and S. Dutta and R. Maitra are with the Department of Statistics, all at Iowa State University, Ames, Iowa 50011, USA. e-mail: {kdorman,somakd,maitra}@iastate.edu.

3) *Assessing variability in handwritten digits*: The Modified National Institute of Standards and Technology (MNIST) database [23] has 70,000 normalized and anti-aliased 28×28 bitmap images of handwritten digits of 0 through 9, written by 500 writers. The standardization of each pixel value to the interval $[0, 255]$, as a consequence of the digitization of the image, means that the raw photon value of each image pixel is no longer available. The loss of a meaningful absolute scale for the image suggests use of correlation as a similarity measure. This similarity measure is akin to normalizing each image to lie on the unit sphere. Characterizing inter-pixel relationships can summarize variability in handwritten digits but again, requires a distribution richer than the Langevin for the same reasons as before. We investigate this application further in Section IV-C.

4) *Identifying genetic pathways underlying cancer*: The Cancer Genome Atlas (TCGA) dataset provides messenger ribonucleic acid (mRNA) sequencing data of tumor samples from more than 11,000 patients collected over a 12-year period. After initial processing, each tumor has gene compositional data, where each observation lies on a simplex, and a square root transformation on each feature maps the observation to lie on a unit sphere [24]. It is expected that a few groups of genes can explain variability between the tumor samples (and patients) and that identification of such gene groups could lead to future diagnostic tools and treatments [25]. Once again, however, such relationships cannot be modeled by the Langevin distribution with its lack of flexible relationships between coordinates. We study this application in detail in Section IV-D.

Our four showcase applications point to the inadequacy of the Langevin distribution in characterizing heterogeneity and relationships between the observed variables that lie on a unit sphere. A more general approach to modeling data on a sphere involves taking the inverse stereographic projection of a general multivariate normal distribution [26], [27]. However, this approach is not practical in high dimensions: indeed, in their application, [27] use *a priori* dimension reduction (into the first three principal components) on the raw data as a preprocessing step before modeling and analysis. Other distributions such as the complex Bingham [28], Fisher-Bingham [29] and the real/complex Watson distributions [30], [31] also suffer from intractability with dimensions greater than three.

A more flexible distributional family arises from the projected normal (PN) distribution that is obtained by radial projection of the multivariate normal (MVN) distribution onto the unit sphere [4]. In general, the PN density does not have a closed-form expression. [32] and [33] provided Bayesian inference for this model in two and higher dimensions, respectively, under the (mild) constraint that the first element of the dispersion matrix parameter of the projected normal density is unity. The structure of this dispersion matrix parameter is of interest in many applications, so we investigate if a small number of latent factors can explain the variability in the (observed) data on a sphere. Our approach posits parameter estimation from a projected normal distribution as a missing data problem, where the complete data is from the generative MVN distribution that we specify in terms of a factor model. Two Alternating Expectation Conditional Maximization (AECM) algorithms [34] are developed for parameter estimation within our framework. Because our interest stems from high-dimensional problems, we also develop accelerated implementations that incorporate squared iterative (SQUAREM) methods [35] to achieve superlinear convergence.

The remainder of this paper is organized as follows. Section II develops the factor model and analysis for data on a sphere (FADS) and proposes two novel AECM algorithms called FADS-D (Expectation-Maximization, *i.e.* EM, with a duet of latent variables) and FADS-P (EM with one latent variable and a profile maximization step) for model-fitting. We use the extended Bayesian Information Criterion (eBIC) of [36] to decide on the number of factors. Section III evaluates the performance of FADS-P and FADS-D in simulation experiments. We next apply our methodology to the motivating applications of Section I-A. Section V discusses possible extensions and future work. An online supplement, with sections, tables, theorems and figures referenced here with the prefix ‘‘S’’, is available.

II. METHODOLOGY

A. Background and preliminary development

1) *The projected normal (PN) distribution*: A popular method of constructing probability distributions on the unit sphere is by radially projecting a multivariate distribution, typically Gaussian and has been well-studied in low-dimensional problems by [4, p. 178], [37], [38], and, from a Bayesian perspective, by [32] and [33]. The PN distribution $\mathcal{PN}_p(\boldsymbol{\mu}, \boldsymbol{\Sigma})$ on the p -unit sphere \mathcal{S}_{p-1} is defined as the distribution of $\mathbf{Y}/\|\mathbf{Y}\|$ where \mathbf{Y} has an MVN distribution with mean $\boldsymbol{\mu}$ and covariance matrix $\boldsymbol{\Sigma}$. Consequently, the $\mathcal{PN}_p(\boldsymbol{\mu}, \boldsymbol{\Sigma})$ density function is

$$f(\mathbf{x}; \boldsymbol{\mu}, \boldsymbol{\Sigma}) = (2\pi)^{-\frac{p}{2}} |\boldsymbol{\Sigma}|^{-\frac{1}{2}} \exp \left\{ -\frac{\boldsymbol{\mu}^\top \boldsymbol{\Sigma}^{-1} \boldsymbol{\mu}}{2} + \frac{m^2}{2v} \right\} \int_0^\infty R^{p-1} \exp \left\{ -\frac{1}{2v} (R - m)^2 \right\} dR, \quad (1)$$

where $m = \mathbf{x}^\top \boldsymbol{\Sigma}^{-1} \boldsymbol{\mu} / \mathbf{x}^\top \boldsymbol{\Sigma}^{-1} \mathbf{x}$, $v = 1 / \mathbf{x}^\top \boldsymbol{\Sigma}^{-1} \mathbf{x}$ (see Theorem S1). The integral in (1) arises from integrating out the unobserved length $R = \|\mathbf{Y}\|$ and is proportional to the p th raw moment of a univariate normal distribution truncated above zero. However, this family of distributions is not identifiable [4], so there is need for further constraints, such as fixing a diagonal entry of $\boldsymbol{\Sigma}$ or, more commonly, setting $\boldsymbol{\mu} \in \mathcal{S}_{p-1}$ that we adopt in this work. The matrix $\boldsymbol{\Sigma}$ flexibly models the dependence among coordinates, allowing different shapes and orientations. For example, Fig. 1 shows the isodensity lines of a 3D PN distribution with the same $\boldsymbol{\mu}$ but three different $\boldsymbol{\Sigma}$ s. With spherical $\boldsymbol{\Sigma}$, the isodensity lines on the surface of the sphere are circular, but for the other two heteroscedastic cases, we obtain ellipsoids of different eccentricities and orientations. [37] provide method-of-moments estimators for the parameters of the PN distribution but this method is impractical for high

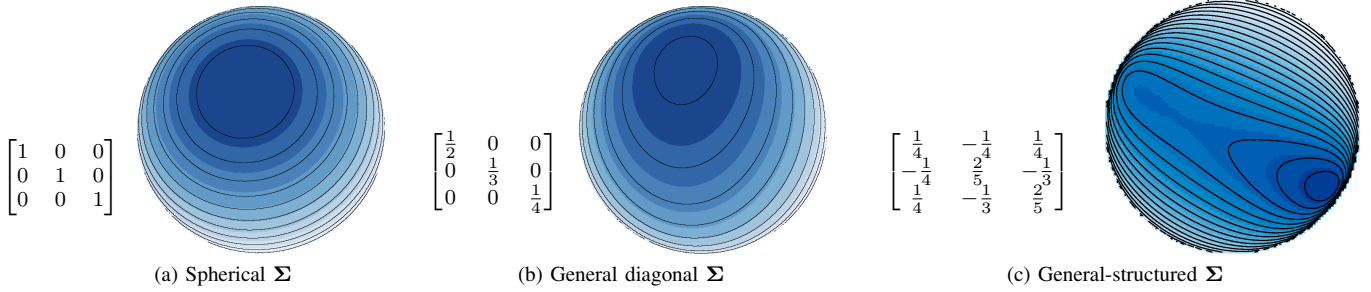


Fig. 1: Sample 3D PN densities (with higher values in darker shades) for three different Σ s.

dimensions, especially when the sample size is relatively small. An alternative approach to specifying general distributions on the sphere is by stereographic projection of the MVN distribution [27]. Both approaches result in multimodal densities as the diagonal entries of Σ increase. However, the stereographic projection approach is not easily analyzed in high dimensions, so [27] suggest reducing the dimensionality of the MVN through principal components analysis before applying stereographic projection. We provide computationally efficient EM algorithms for maximum likelihood (ML) estimators for the parameters of the PN distribution that can be used in high dimensions. Our approach also decomposes Σ into a factor structure, allowing for interpretation and further understanding of the variability in a dataset. We describe our factor model setup next.

2) *A latent factor model for the PN distribution:* Let $\mathbf{X}_1, \mathbf{X}_2, \dots, \mathbf{X}_n$ be independent identically distributed (i.i.d.) realizations from (1). Our latent factor model assumes $\mathbf{X}_i = \mathbf{Y}_i / \|\mathbf{Y}_i\|$, where the generative latent variables \mathbf{Y}_i have the decomposition

$$\mathbf{Y}_i = \boldsymbol{\mu} + \boldsymbol{\Lambda} \mathbf{Z}_i + \boldsymbol{\epsilon}_i, \quad i = 1, 2, \dots, n \quad (2)$$

and $\boldsymbol{\Lambda}$ is a $p \times q$ matrix called the factor loading matrix with rank q , \mathbf{Z}_i s are latent factors of dimension q and $\boldsymbol{\epsilon}_i$ s are residual noise vectors. Typically, $q \ll \min(n, p)$ and so (2) explains the variability in the \mathbf{Y}_i s in terms of a few (q) underlying latent factors. Usually, \mathbf{Z}_i s are assumed independent $\mathcal{N}_q(\mathbf{0}, \mathbf{I})$ and $\boldsymbol{\epsilon}_i$ s independent $\mathcal{N}_p(\mathbf{0}, \boldsymbol{\Psi})$ random vectors, where $\boldsymbol{\Psi}$ is a diagonal matrix with positive entries called the uniquenesses. Hence, the covariance matrix Σ admits a lower-dimensional representation: $\Sigma = \boldsymbol{\Lambda} \boldsymbol{\Lambda}^\top + \boldsymbol{\Psi}$. Parameter estimation in (2) has received attention [26], [39], [40], [41], [42], [43] over several decades, with recent work [44] providing near-instantaneous solutions even for very high dimensions.

The Gaussian factor model (2) is not invariant to orthogonal transformation [26], [42] unless all uniquenesses are equal (i.e. $\boldsymbol{\Psi} = \sigma^2 \mathbf{I}_p$ for some $\sigma^2 > 0$). Also, (2) is not identifiable because both $\boldsymbol{\Lambda}$ and $\boldsymbol{\Lambda} \mathbf{Q}$ give rise to the same model for any orthogonal matrix \mathbf{Q} and so additional constraints are needed for identifiability. For computational simplicity, we assume that $\boldsymbol{\Lambda}^\top \boldsymbol{\Psi}^{-1} \boldsymbol{\Lambda}$ is diagonal with decreasing diagonal entries. However, for better interpretability, and as is standard in traditional factor analysis, we present estimates of $\boldsymbol{\Lambda}$ after applying some appropriate orthogonal (e.g. varimax, quartimax or oblimin) rotation [45].

B. Estimation of parameters

The PN factor model of Section II-A2 has two generative latent components – the lengths $R_i = \|\mathbf{Y}_i\|$ and the factors \mathbf{Z}_i , $i = 1, 2, \dots, n$. Given q and these inherent latencies, the EM algorithm provides a natural way to obtain the ML estimators of $\boldsymbol{\mu}$, $\boldsymbol{\Lambda}$ and $\boldsymbol{\Psi}$. But vanilla EM is slow to converge, so we develop an AECM algorithm [34] for parameter estimation using the latent components (R_i, \mathbf{Z}_i)s. However, [44] recently showed a matrix-free profile likelihood approach to be more computationally efficient than EM [43] for the Gaussian factor model. Building on that approach, we develop a AECM algorithm, where the expectation step (E-step) only integrates over the latent R_i s, while the conditional maximization step (CM-step) maximizes over $\boldsymbol{\mu}$ with the latent factor model parameters estimated after profiling the expected complete log-likelihood. Our algorithms are further accelerated by SQUAREM [35] to achieve superlinear convergence.

1) *An AECM algorithm with a duet of latent variables:* The EM algorithm for ML estimation in a Gaussian factor model [46] can be naturally extended to the PN factor model by considering both $\mathbf{R} = (R_1, R_2, \dots, R_n)$ and $\mathbf{Z} = [\mathbf{Z}_1, \mathbf{Z}_2, \dots, \mathbf{Z}_n]$ as missing data. Then the Q -function, that is, the conditional expectation of the complete data log-likelihood given the data \mathbf{X} , is

$$Q_D(\boldsymbol{\mu}, \boldsymbol{\Lambda}, \boldsymbol{\Psi}; \boldsymbol{\mu}_t, \boldsymbol{\Lambda}_t, \boldsymbol{\Psi}_t) = c - \frac{1}{2} n [\log \det \boldsymbol{\Psi} + \text{Tr} \{ \boldsymbol{\Psi}^{-1} \mathbb{E}_{\mathbf{Z}, \mathbf{R} | \mathbf{X}}(\mathbf{S}_{\mathbf{Z}, \mathbf{R}}) \}], \quad (3)$$

where c is a constant free of $\boldsymbol{\mu}$, $\boldsymbol{\Lambda}$ and $\boldsymbol{\Psi}$, and $\mathbb{E}_{\mathbf{Z}, \mathbf{R} | \mathbf{X}}(\mathbf{S}_{\mathbf{Z}, \mathbf{R}})$ is the conditional expectation of $\mathbf{S}_{\mathbf{Z}, \mathbf{R}} = n^{-1} \sum_{i=1}^n (R_i \mathbf{X}_i - \boldsymbol{\mu} - \boldsymbol{\Lambda} \mathbf{Z}_i)(R_i \mathbf{X}_i - \boldsymbol{\mu} - \boldsymbol{\Lambda} \mathbf{Z}_i)^\top$ given \mathbf{X} , at the current parameter values $(\boldsymbol{\mu}_t, \boldsymbol{\Lambda}_t, \boldsymbol{\Psi}_t)$. The E-step needs this conditional expectation, but it is straightforward to show (Section S1.5) that the conditional distribution of \mathbf{Z}_i given \mathbf{R} and \mathbf{X} at the current parameter values $(\boldsymbol{\mu}_t, \boldsymbol{\Lambda}_t, \boldsymbol{\Psi}_t)$ is $\mathcal{N}_q(\boldsymbol{\Lambda}_t^\top (\boldsymbol{\Lambda}_t \boldsymbol{\Lambda}_t^\top + \boldsymbol{\Psi}_t)^{-1} (R_i \mathbf{X}_i - \boldsymbol{\mu}_t), (\mathbf{I} + \boldsymbol{\Lambda}_t^\top \boldsymbol{\Psi}_t^{-1} \boldsymbol{\Lambda}_t)^{-1})$. Further, the conditional expectations of R_i and R_i^2 given \mathbf{X} are $\mathbb{E}_{R_i | \mathbf{X}_i}(R_i) = \mathcal{I}_p(m_i, v_i) / \mathcal{I}_{p-1}(m_i, v_i)$ and $\mathbb{E}_{R_i | \mathbf{X}_i}(R_i^2) = \mathcal{I}_{p+1}(m_i, v_i) / \mathcal{I}_{p-1}(m_i, v_i)$

where $m_i = \mathbf{X}_i^\top (\mathbf{\Lambda}_t \mathbf{\Lambda}_t^\top + \mathbf{\Psi}_t)^{-1} \boldsymbol{\mu}_t / \mathbf{X}_i^\top (\mathbf{\Lambda}_t \mathbf{\Lambda}_t^\top + \mathbf{\Psi}_t)^{-1} \mathbf{X}_i$, $v_i = 1 / \mathbf{X}_i^\top (\mathbf{\Lambda}_t \mathbf{\Lambda}_t^\top + \mathbf{\Psi}_t)^{-1} \mathbf{X}_i$ at the current parameter values $(\boldsymbol{\mu}_t, \mathbf{\Lambda}_t, \mathbf{\Psi}_t)$, and

$$\mathcal{I}_k(m, v) := \int_0^\infty R^k \exp \left\{ -\frac{1}{2v} (R - m)^2 \right\} dR, \quad (4)$$

for $k \geq 0$. We discuss fast methods for numerically computing these quantities in Section II-B3.

Unlike for Gaussian factor models, the estimate of $\boldsymbol{\mu}$ cannot be profiled out but is part of the M-step. Further, there is no closed-form solution for maximizing $Q_D(\cdot)$ with respect to (w.r.t.) $\boldsymbol{\mu}$, $\mathbf{\Lambda}$ and $\mathbf{\Psi}$ simultaneously, nor are there easy numerical schemes to maximize $Q_D(\cdot)$. So we partition the parameter space naturally in terms of $\{\boldsymbol{\mu}\}$, $\{\mathbf{\Lambda}\}$, $\{\mathbf{\Psi}\}$ and conditionally maximize $Q_D(\cdot)$ w.r.t. each set of parameters, in turn, while fixing the other sets of parameters at their current values. We alternate an E-step with each CM-step that we now discuss individually. It is important to note that all CM-steps in our AECM algorithm have closed-form solutions. The E-step has two sets (or a duet) of latent variables, so we use FADS-D to specify this algorithm.

The CM-step update for $\boldsymbol{\mu}$ at the $(t+1)$ th iteration is $\boldsymbol{\mu}_{t+1} = \arg \max_{\boldsymbol{\mu}} Q_D(\boldsymbol{\mu}, \mathbf{\Lambda}_t, \mathbf{\Psi}_t; \boldsymbol{\mu}_t, \mathbf{\Lambda}_t, \mathbf{\Psi}_t)$ subject to the constraint $\|\boldsymbol{\mu}\| = 1$. This CM-step has the closed-form solution

$$\boldsymbol{\mu}_{t+1} = (\mathbf{I} + \lambda \mathbf{\Psi}_t)^{-1} \mathbf{b}_t, \quad (5)$$

where $\mathbf{b}_t = \frac{1}{n} \sum_{i=1}^n \{ \mathbb{E}_{R_i | \mathbf{X}_i} (R_i) \mathbf{X}_i - \mathbf{\Lambda}_t \mathbb{E}_{\mathbf{Z}_i | \mathbf{X}_i} (\mathbf{Z}_i) \}$ and λ is the Lagrange multiplier. The following proposition shows that λ can be computed easily, and so $\boldsymbol{\mu}_{t+1}$ has a unique closed-form solution for $\boldsymbol{\mu}_{t+1} = \arg \max_{\boldsymbol{\mu}} Q_D(\boldsymbol{\mu}, \mathbf{\Lambda}_t, \mathbf{\Psi}_t; \boldsymbol{\mu}_t, \mathbf{\Lambda}_t, \mathbf{\Psi}_t)$ subject to the constraint $\|\boldsymbol{\mu}\| = 1$.

Proposition 1. *The global maximizer of $\boldsymbol{\mu} \mapsto Q_D(\boldsymbol{\mu}, \mathbf{\Lambda}_t, \mathbf{\Psi}_t)$ is given by (5), where λ is a root of $f(u) = \mathbf{b}_t^\top (\mathbf{I} + u \mathbf{\Psi}_t)^{-2} \mathbf{b}_t - 1$. Moreover, if $\|\mathbf{b}_t\| > 1$, then λ is the unique root of $f(u)$ between 0 and $\mathbf{b}_t^\top \mathbf{\Psi}_t^{-1} \mathbf{b}_t / 2$, and otherwise the unique negative root between $(|\mathbf{b}^*|/2 - 1)/\psi^*$ and 0, where ψ^* is the largest diagonal entry of $\mathbf{\Psi}_t$ and \mathbf{b}^* is the corresponding entry in \mathbf{b}_t .*

Proof. The proposition is a corollary of Theorem S2 in Section S1.2 with $\mathbf{B} = \mathbf{\Psi}$. \square

For the CM-step for $\mathbf{\Lambda}$, we maximize $Q_D(\boldsymbol{\mu}_{t+1}, \mathbf{\Lambda}, \mathbf{\Psi}_t; \boldsymbol{\mu}_{t+1}, \mathbf{\Lambda}_t, \mathbf{\Psi}_t)$ w.r.t. $\mathbf{\Lambda}$ at the current values of the other parameters, that is at $\boldsymbol{\mu}_{t+1}$ and $\mathbf{\Psi}_t$ to get the update

$$\mathbf{\Lambda}_{t+1} = \left[\sum_{i=1}^n \mathbb{E}_{\mathbf{Z}_i, R_i | \mathbf{X}_i} \{ (R_i \mathbf{X}_i - \boldsymbol{\mu}_{t+1}) \mathbf{Z}_i^\top \} \right] \left\{ \sum_{i=1}^n \mathbb{E}_{\mathbf{Z}_i | \mathbf{X}_i} (\mathbf{Z}_i \mathbf{Z}_i^\top) \right\}^{-1}, \quad (6)$$

where the conditional expectations are at the current parameter values $\{\boldsymbol{\mu}_{t+1}, \mathbf{\Lambda}_t, \mathbf{\Psi}_t\}$.

Finally, the CM-step for $\mathbf{\Psi}$ maximizes $Q_D(\boldsymbol{\mu}_{t+1}, \mathbf{\Lambda}_{t+1}, \mathbf{\Psi}; \boldsymbol{\mu}_{t+1}, \mathbf{\Lambda}_{t+1}, \mathbf{\Psi}_t)$ w.r.t. $\mathbf{\Psi}$ while keeping fixed the values of the other parameters at $\boldsymbol{\mu}_{t+1}$ and $\mathbf{\Lambda}_{t+1}$. The CM-step update is then

$$\mathbf{\Psi}_{t+1} = \text{diag} \left[\frac{1}{n} \sum_{i=1}^n \mathbb{E}_{R_i, \mathbf{Z}_i | \mathbf{X}_i} \{ (R_i \mathbf{X}_i - \boldsymbol{\mu}_{t+1} - \mathbf{\Lambda}_{t+1} \mathbf{Z}_i) (R_i \mathbf{X}_i - \boldsymbol{\mu}_{t+1} - \mathbf{\Lambda}_{t+1} \mathbf{Z}_i)^\top \} \right], \quad (7)$$

where the conditional expectation is at the current parameter values $\{\boldsymbol{\mu}_{t+1}, \mathbf{\Lambda}_{t+1}, \mathbf{\Psi}_t\}$.

2) *A faster AECM algorithm with profiling:* The methodology of Section II-B1 has two sets of latent variables in the lengths R_i s and the factors \mathbf{Z}_i s. The latter also arise in the case of EM methods for Gaussian factor models, but can be eliminated by employing matrix-free profile likelihood maximization [44]. We propose to speed up our AECM algorithm by incorporating these methods. We drop \mathbf{Z}_i s from our erstwhile duet and only consider R_i s as our latent variables. Then the Q -function is

$$Q_P(\boldsymbol{\mu}, \mathbf{\Lambda}, \mathbf{\Psi}; \boldsymbol{\mu}_t, \mathbf{\Lambda}_t, \mathbf{\Psi}_t) = c - \frac{n}{2} \{ \log \det(\mathbf{\Lambda} \mathbf{\Lambda}^\top + \mathbf{\Psi}) + \text{Tr}(\mathbf{\Lambda} \mathbf{\Lambda}^\top + \mathbf{\Psi})^{-1} \mathbb{E}_{\mathbf{R} | \mathbf{X}}(\mathbf{S}_R) \}, \quad (8)$$

where c is a constant free of $\boldsymbol{\mu}$, $\mathbf{\Lambda}$ and $\mathbf{\Psi}$, and $\mathbb{E}_{\mathbf{R} | \mathbf{X}}(\mathbf{S}_R)$ is the conditional expectation of $\mathbf{S}_R = n^{-1} \sum_{i=1}^n (R_i \mathbf{X}_i - \boldsymbol{\mu})(R_i \mathbf{X}_i - \boldsymbol{\mu})^\top$ at the current parameter values $(\boldsymbol{\mu}_t, \mathbf{\Lambda}_t, \mathbf{\Psi}_t)$. The calculation of the conditional expectation $\mathbb{E}_{\mathbf{R} | \mathbf{X}}(\mathbf{S}_R)$ involves the same conditional expectations of R_i and R_i^2 given \mathbf{X} as in FADS-D and are computed similarly. We now discuss the CM-steps of the AECM algorithm, where we partition the parameter space into $\{\boldsymbol{\mu}\}$ and $\{\mathbf{\Lambda}, \mathbf{\Psi}\}$.

The CM-step for $\boldsymbol{\mu}$ (at the $(t+1)$ th cycle) involves maximizing $Q_P(\boldsymbol{\mu}, \mathbf{\Lambda}_t, \mathbf{\Psi}_t; \boldsymbol{\mu}_t, \mathbf{\Lambda}_t, \mathbf{\Psi}_t)$ as a function of $\boldsymbol{\mu}$ subject to the constraint $\|\boldsymbol{\mu}\| = 1$. Analogous to Proposition 1, a unique closed-form solution for the CM-step for $\boldsymbol{\mu}$ can be obtained through the following

Proposition 2. *The global maximizer of $\boldsymbol{\mu} \mapsto Q_P(\boldsymbol{\mu}, \mathbf{\Lambda}_t, \mathbf{\Psi}_t)$ is $\boldsymbol{\mu}_{t+1} = (\mathbf{I} + \lambda \boldsymbol{\Sigma}_t)^{-1} \mathbf{c}_t$, where $\mathbf{c}_t = n^{-1} \sum_{i=1}^n \mathbf{X}_i \mathbb{E}(R_i | \mathbf{X}_i, \boldsymbol{\mu}_t, \mathbf{\Lambda}_t, \mathbf{\Psi}_t)$, $\boldsymbol{\Sigma}_t = \mathbf{\Lambda}_t \mathbf{\Lambda}_t^\top + \mathbf{\Psi}_t$ and λ is a root of $g(u) = \mathbf{c}_t^\top (\mathbf{I} + u \boldsymbol{\Sigma}_t)^{-2} \mathbf{c}_t - 1$. Moreover, if $\|\mathbf{c}_t\| > 1$, then λ is the unique root of $g(u)$ between 0 and $\mathbf{c}_t^\top \boldsymbol{\Sigma}_t^{-1} \mathbf{c}_t / 2$, otherwise it is the unique negative root between $(|\mathbf{v}_*^\top \mathbf{c}_t| / 2 - 1) / \sigma^*$ and 0, where σ^* is the largest eigenvalue of $\boldsymbol{\Sigma}_t$ with eigenvector \mathbf{v}_* .*

Proof. The proposition follows as a corollary to Theorem S2 in Section S1.2 with $\mathbf{B} = \boldsymbol{\Sigma}$. \square

The root λ in Proposition 2 can be computed by bisection while \mathbf{v}_* can be computed using a restarted Lanczos algorithm, as seen shortly in Section II-B3. Also, the inverses of Σ_t or $\mathbf{I} + \lambda \Sigma_t$ are computed using the Sherman-Morrison-Woodbury identity [47].

Given $\boldsymbol{\mu}_{t+1}$ and \mathbf{X}_i , $i = 1, 2, \dots, n$, we obtain $\mathbb{E}(R_i | \mathbf{X}_i)$ and $\mathbb{E}(R_i^2 | \mathbf{X}_i)$ and let

$$\tilde{\mathbf{S}}_t = \mathbb{E}_{\mathbf{R}|\mathbf{X}}(\mathbf{S}_R) \Big|_{\boldsymbol{\mu}=\boldsymbol{\mu}_{t+1}} \equiv \frac{1}{n} \sum_{i=1}^n \mathbb{E}_{R_i|\mathbf{X}_i} \{ (R_i \mathbf{X}_i - \boldsymbol{\mu}_{t+1})(R_i \mathbf{X}_i - \boldsymbol{\mu}_{t+1})^\top \}$$

at the current parameter values. With $\boldsymbol{\mu}$ held fixed at $\boldsymbol{\mu}_{t+1}$, maximizing (8) w.r.t. $\boldsymbol{\Lambda}$ and $\boldsymbol{\Psi}$ is equivalent to maximizing the log-likelihood of a Gaussian factor model where the mean is profiled out and the ‘‘sample covariance’’ matrix is $\tilde{\mathbf{S}}_t$. Therefore, we jointly update $\boldsymbol{\Lambda}$ and $\boldsymbol{\Psi}$ by following [44] and profiling out $\boldsymbol{\Lambda}$, using the common (in Gaussian factor analysis) and computationally useful identifiability constraint on $\boldsymbol{\Lambda}$ that the signal matrix $\boldsymbol{\Gamma} = \boldsymbol{\Lambda}^\top \boldsymbol{\Psi}^{-1} \boldsymbol{\Lambda}$ is diagonal with non-increasing diagonal entries. This scale-invariant constraint is determined up to sign in the columns of $\boldsymbol{\Lambda}$. Under this constraint, $\boldsymbol{\Lambda}$ is profiled out from $Q_P(\boldsymbol{\mu}_{t+1}, \boldsymbol{\Lambda}, \boldsymbol{\Psi}; \boldsymbol{\mu}_{t+1}, \boldsymbol{\Lambda}_t, \boldsymbol{\Psi}_t)$ for a given $\boldsymbol{\Psi}$ as per the following

Proposition 3. *For a positive-definite diagonal matrix $\boldsymbol{\Psi}$, let $\theta_1 \geq \theta_2 \geq \dots \geq \theta_q$, be the q largest eigenvalues of $\mathbf{W} = \boldsymbol{\Psi}^{-1/2} \tilde{\mathbf{S}}_t \boldsymbol{\Psi}^{-1/2}$. Let the columns of \mathbf{V}_q store the eigenvectors corresponding to these eigenvalues. Then the function $Q_P(\boldsymbol{\mu}_{t+1}, \boldsymbol{\Lambda}, \boldsymbol{\Psi}; \boldsymbol{\mu}_{t+1}, \boldsymbol{\Lambda}_t, \boldsymbol{\Psi}_t)$ is maximized w.r.t. $\boldsymbol{\Lambda}$ at $\hat{\boldsymbol{\Lambda}} = \boldsymbol{\Psi}^{1/2} \mathbf{V}_q \boldsymbol{\Delta}$, where $\boldsymbol{\Delta}$ is a $q \times q$ diagonal matrix with i th diagonal entry as $[\max(\theta_i - 1, 0)]^{1/2}$. The profile Q -function is*

$$Q_p(\boldsymbol{\Psi}) \doteq c' - \frac{n}{2} \{ \log \det \boldsymbol{\Psi} + \text{Tr} \boldsymbol{\Psi}^{-1} \tilde{\mathbf{S}}_t + \sum_{i=1}^q (\log \theta_i - \theta_i + 1) \}, \quad (9)$$

where c' is a constant free of $\boldsymbol{\Psi}$. Further, $\nabla Q_p(\boldsymbol{\Psi}) = -\frac{1}{2}n \text{diag}(\hat{\boldsymbol{\Lambda}} \hat{\boldsymbol{\Lambda}}^\top + \boldsymbol{\Psi} - \tilde{\mathbf{S}}_t)$.

Proof. See Section S1.3. □

Our algorithm here involves profiling in the second CM-step, so we call it FADS-P. We use the limited-memory Broyden-Fletcher-Goldfarb-Shanno quasi-Newton algorithm [48] with box-constraints (L-BFGS-B) to maximize (9). Instead of the exact Hessian matrix, this quasi-Newton algorithm uses values of $Q_p(\boldsymbol{\Psi})$ and $\nabla Q_p(\boldsymbol{\Psi})$ from the last few (typically five) iterations to find an effective approximation to the exact Newton-step, thereby reducing storage costs from $O(p^2)$ to $O(p)$. Having obtained $\boldsymbol{\Psi}_{t+1} = \arg \max Q_p(\boldsymbol{\Psi})$, we use Proposition 3 to compute the eigenvalues and eigenvectors of $\boldsymbol{\Psi}_{t+1}^{-1/2} \tilde{\mathbf{S}}_t \boldsymbol{\Psi}_{t+1}^{-1/2}$ and update $\boldsymbol{\Lambda}_{t+1} = \boldsymbol{\Psi}_{t+1}^{1/2} \mathbf{V}_q \boldsymbol{\Delta}$.

We conclude with a few remarks on the CM-update of $\boldsymbol{\Psi}$. The function $Q_p(\boldsymbol{\Psi})$ in (9) depends on $\tilde{\mathbf{S}}_t$ only through the q largest eigenvalues of \mathbf{W} , so for $Q_p(\boldsymbol{\Psi})$ and $\nabla Q_p(\boldsymbol{\Psi})$, we need to compute only the q largest eigenvalues and corresponding eigenvectors of \mathbf{W} . For $q \ll \min(n, p)$, the largest eigenvalues and eigenvectors are speedily computed using the restarted Lanczos algorithm, with constraints on $\boldsymbol{\Psi}$ (e.g., $\boldsymbol{\Psi} = \sigma^2 \mathbf{I}_p$, $\sigma^2 > 0$) easily incorporated. Also, $\nabla Q_p(\boldsymbol{\Psi})$ is available in closed-form, enabling a check for first-order optimality. Finally, $Q_p(\boldsymbol{\Psi})$ is expressed in terms of $\tilde{\mathbf{S}}_t$, but ML estimators are scale-equivariant, so each iteration of FADS-P estimates $\boldsymbol{\Lambda}$ and $\boldsymbol{\Psi}$ using the correlation matrix and scales the estimates back to that of $\tilde{\mathbf{S}}_t$.

3) *Implementation via fast statistical computations:* We want our FADS algorithms to also be used for datasets with large n or p , as in our applications, so we now discuss and investigate practical ways to speed up computations.

a) *Computation of log-likelihood and conditional expectations:* Both the log-likelihood (1) and the conditional expectations require computing (4) for $k \in \{p-1, p, p+1\}$. To reduce clutter, we write $\mathcal{I}_k \equiv \mathcal{I}_k(m, v)$. Integration by parts yields the recurrence relation [37]

$$\mathcal{I}_{k+2} = m \mathcal{I}_{k+1} + (k+1)v \mathcal{I}_k. \quad (10)$$

However, this recurrence relation is vulnerable to numerical overflow for large p , so we derive (Section S1.4) a recurrence relation for the ratio

$$\frac{\mathcal{I}_{k+2}}{\mathcal{I}_{k+1}} = m + (k+1)v \frac{\mathcal{I}_k}{\mathcal{I}_{k+1}}. \quad (11)$$

Together, (10) and (11) also yield $\mathcal{I}_{k+2}/\mathcal{I}_k = (k+1)v + m \mathcal{I}_{k+1}/\mathcal{I}_k$. When $m > 0$, the recurrence relation (11) is numerically stable and computed very quickly, even for large k . However, for $m < 0$, both (10) and (11) are unstable and often yield negative values for \mathcal{I}_k with $k > 10$. So, for $m < 0$, we use quadrature to compute \mathcal{I}_k , for $k \in \{p-1, p, p+1\}$, using the fact that the integrand in (4) is strictly log-concave and maximized at $\varrho = (m + \sqrt{m^2 + 4vk})/2$. We write

$$\log \mathcal{I}_k = k \log \varrho - \frac{1}{2v} (\varrho - m)^2 + \log \int_0^\infty \left(\frac{R}{\varrho} \right)^k \exp \left\{ -\frac{1}{2v} (R - \varrho)(R + \varrho - 2m) \right\} dR. \quad (12)$$

The integrand is bounded above by unity so we can easily find (e.g., using bisection) two quantities $0 < \underline{\varrho} < \bar{\varrho}$ where the integrand is less than some small value (e.g., 10^{-15}). The integration in (12) is by non-adaptive Gauss-Kronrod quadrature over $[\underline{\varrho}, \bar{\varrho}]$ with 10, 21, 43 and 87 points [49]: in our experiments, 43 points gave high numerical accuracy.

b) *Computation of partial eigenvalues and eigenvectors:* We can obtain the q largest eigenvalues and eigenvectors of \mathbf{W} via the implicitly restarted Lanczos algorithm [50]. Suppose that $m = \max\{2q + 1, 20\}$ and that $\mathbf{f}_1 \in \mathbb{R}^p$ is any vector with $\|\mathbf{f}_1\| = 1$ and initialize $\mathbf{F}_1 = \mathbf{f}_1$. We then employ the Lanczos iterations [51] as follows. For $k = 1, 2, \dots, m$,

- Compute $\mathbf{u}_k = \mathbf{W}\mathbf{f}_k$ and $\alpha_k = \mathbf{f}_k^\top \mathbf{u}_k$.
- Compute $\mathbf{r}_k = \mathbf{u}_k - \alpha_k \mathbf{f}_k - \beta_{k-1} \mathbf{f}_{k-1}$ (assuming $\beta_0 = 0$ and $\mathbf{f}_0 = \mathbf{0}$).
- Let $\beta_k = \|\mathbf{r}_k\|$ and if $k < q$ and $\beta_k \neq 0$, compute $\mathbf{f}_{k+1} = \frac{\mathbf{r}_k}{\beta_k}$ and set $\mathbf{F}_{k+1} = [\mathbf{F}_k, \mathbf{f}_{k+1}]$.

Suppose that \mathbf{T}_m is the $m \times m$ symmetric tridiagonal matrix with diagonal entries $\alpha_1, \alpha_2, \dots, \alpha_m$ and j th off-diagonal entries β_j for $j = 1, \dots, m - 1$. We compute the eigenvalues $e_1 > e_2 > \dots > e_m$ of \mathbf{T}_m with eigenvectors $\mathbf{g}_1, \mathbf{g}_2, \dots, \mathbf{g}_m$ via a Sturm sequencing algorithm [52]. Also let $\mathbf{v}_j = \mathbf{F}_m \mathbf{g}_j$, for $1 \leq j \leq m$. The e_j 's and \mathbf{v}_j 's are called Ritz values and Ritz vectors of \mathbf{W} . It can be shown that $\|\mathbf{W}\mathbf{v}_j - \mathbf{v}_j e_j\| = \beta_m |g_{j,m}|$, for $g_{j,m}$ the m th entry of vector \mathbf{g}_j , for $j = 1, 2, \dots, m$. The algorithm stops if

$$\beta_m \max_{1 \leq j \leq m} |g_{j,m}| < \delta \quad (13)$$

for some prespecified tolerance δ and e_1, \dots, e_q and $\mathbf{v}_1, \mathbf{v}_2, \dots, \mathbf{v}_q$ are accurate approximations of the q largest eigenvalues and corresponding eigenvectors of \mathbf{W} .

However, in practice, more iterations are needed for the Ritz vectors and Ritz values to converge to the eigenvalues and eigenvectors of \mathbf{W} , so [50] suggests implicitly restarting the Lanczos algorithm and also shifting the spectrum of the symmetric tridiagonal matrices iteratively to force the new residuals \mathbf{r}_m to zero, thereby accelerating the convergence rate. So we compute the QR-decompositions: $\mathbf{T}_m - e_j \mathbf{I}_m = \mathbf{Q}_j \tilde{\mathbf{R}}_j$, for $j = q + 1, \dots, m$, let $\tilde{\mathbf{Q}} = \mathbf{Q}_{q+1} \mathbf{Q}_{q+2} \dots \mathbf{Q}_m$ and reset $\mathbf{F}_m = \mathbf{F}_m \tilde{\mathbf{Q}}$ and $\mathbf{T}_m = \tilde{\mathbf{Q}}^\top \mathbf{T}_m \tilde{\mathbf{Q}}$. Then

$$\mathbf{W}\mathbf{F}_q = \mathbf{F}_q \mathbf{T}_q + \beta^* \mathbf{f}_{q+1} \mathbf{e}_q^\top \quad (14)$$

where β^* is the $(q + 1, q)$ th entry of \mathbf{T}_m , \mathbf{e}_q is the q th canonical basis vector in \mathbb{R}^q , and \mathbf{T}_q is the $q \times q$ principal sub-matrix of \mathbf{T}_m [50]. Therefore, (14) is itself a q th-order Lanczos factorization of \mathbf{W} . Next, we “restart” the Lanczos iterations from $k = q + 1, \dots, m$ instead of 1 through m , terminating if (13) is satisfied, and restarting the algorithm otherwise.

The only way \mathbf{W} enters our algorithm is through matrix-vector products $\mathbf{W}\mathbf{f}_k$ that can be computed without storing \mathbf{W} or $\tilde{\mathbf{S}}_t$. Additionally, \mathbf{W} is symmetric, so we do not need separate computations for the left and right singular vectors in partial singular value decomposition using the Lanczos algorithm (as needed in [44]), yielding substantial savings in terms of both compute time and storage. Overall, our algorithm calculates the q largest eigenvalues and eigenvectors with $O(qnp)$ computational cost and $O(qp)$ additional memory.

4) *Initialization:* As with most iterative algorithms, initial values can significantly impact performance of our EM algorithms. We devise methods for initializing $(\boldsymbol{\mu}, \boldsymbol{\Lambda}, \boldsymbol{\Psi})$, borrowing ideas from [53], [54]. Our $\boldsymbol{\mu}$ was simulated from $\mathcal{N}_p(\mathbf{0}, \mathbf{I})$ and l_2 -normalized, while the diagonal entries of $\boldsymbol{\Psi}$ were each i.i.d. $\mathcal{U}(0.2, 0.8)$ draws and the elements of $\boldsymbol{\Lambda}$ were i.i.d. $\mathcal{N}(0, 1)$ realizations. Starting with M such initial values, the AECM algorithm was run for J “short” iterations after which only the $L \leq M$ streams with the highest log-likelihood values were iterated all the way to convergence. The final estimates are those obtained from the run achieving the highest final log-likelihood values. In this paper, we used $(M, J, L) = (1000, 10, 10)$.

C. Choosing q

The factor model explains variability in a large number of variables through a small number (q) of latent factors, so the choice of q is important. There is little theoretical work on the selection of q for Gaussian factor models. The Bayesian information criterion (BIC) of [55] is one possibility, however it does not always perform well in high dimensions [36]. We use eBIC that minimizes $\text{eBIC}(q) = -2 \log \hat{\ell}_q + pq\{\log(n) + 2\gamma \log(p)\}$, with $\gamma = \max\{1 - 1/(2 \log_n(p)), 0\}$, which performs well in our experiments.

D. Estimating the factor scores

Once q has been chosen and the ML estimators of the parameters obtained, we may compute factor scores for use in subsequent analyses. For example, these scores can be used to rank each observational unit on the factors, for post-hoc clustering [56], [57], [58], [59], in scRNA-seq analysis [60], [61], or they can be used as covariates in generalized linear regression models [62], for example, to account for population structure in genome-wide association studies [63], [64], [65]. We extend the approach of [66, p 226–231] to estimate the factor score for the i th observation by minimizing the expected weighted squared error loss $\mathbb{E}\{\|\boldsymbol{\Psi}^{-1/2}(\mathbf{Y}_i - \boldsymbol{\mu} - \boldsymbol{\Lambda}\mathbf{Z}_i)\|^2 | \mathbf{X}_i\}$. The resulting solution is the conditional expectation of Bartlett score with complete data: $\widehat{\mathbf{Z}}_i = (\boldsymbol{\Lambda}^\top \boldsymbol{\Psi}^{-1} \boldsymbol{\Lambda})^{-1} \boldsymbol{\Lambda}^\top \boldsymbol{\Psi}^{-1} \{\mathbb{E}_{R_i | \mathbf{X}_i}(R_i) \mathbf{X}_i - \boldsymbol{\mu}\}$. We use the unobserved \mathbf{Y}_i s instead of \mathbf{X}_i s in the minimization problem because $\boldsymbol{\Psi}$ and $\boldsymbol{\Lambda}$ are estimated on the latent scale. As a result, the factor scores are also estimated on the latent scale. In practice, the ML estimates of the parameters are plugged in, and the value of the conditional expectation $\mathbb{E}_{R_i | \mathbf{X}_i}(R_i)$ at the ML estimates is available as a byproduct of our FADS algorithms.

E. Standard errors of the ML estimates

The standard errors of the ML estimates can be obtained by using the missing information principle [67] when $n \geq (q+2)p$. To that end, suppose that $\Theta = \{\mu, \Lambda, \Psi\}$. The observed information at the ML estimates is given by, $\mathbf{I}_X(\Theta) = (1/n) \sum_{i=1}^n \nabla \mathbf{q}_i \nabla \mathbf{q}_i^\top$, where for $i = 1, 2, \dots, n$ $\nabla \mathbf{q}_i = \mathbb{E}_{R_i | \mathbf{X}_i}(\partial \ell(\mathbf{Y}_i; \Theta) / \partial \Theta)$ is the complete data score statistic and

$$\begin{aligned} \frac{\partial \ell(\mathbf{Y}_i; \Theta)}{\partial \mu} &= (\Lambda \Lambda^\top + \Psi)^{-1} (R_i \mathbf{X}_i - \mu) \\ \frac{\partial \ell(\mathbf{Y}_i; \Theta)}{\partial \Lambda} &= -\frac{1}{2} \left\{ (\Lambda \Lambda^\top + \Psi)^{-1} \Lambda - (\Lambda \Lambda^\top + \Psi)^{-1} (R_i \mathbf{X}_i - \mu) (R_i \mathbf{X}_i - \mu)^\top (\Lambda \Lambda^\top + \Psi)^{-1} \Lambda \right\} \\ \frac{\partial \ell(\mathbf{Y}_i; \Theta)}{\partial \Psi} &= -\frac{1}{2} \text{diag} \left\{ (\Lambda \Lambda^\top + \Psi)^{-1} - (\Lambda \Lambda^\top + \Psi)^{-1} (R_i \mathbf{X}_i - \mu) (R_i \mathbf{X}_i - \mu)^\top (\Lambda \Lambda^\top + \Psi)^{-1} \right\}. \end{aligned}$$

In practice, the ML estimates of the parameters μ, Λ and Ψ are plugged into the above. Further, $\mathbb{E}(R_i | \mathbf{X}_i)$ and $\mathbb{E}(R_i^2 | \mathbf{X}_i)$ at the ML estimates are available as byproducts of the AECM algorithm so these calculations are very easily obtained in the course of the FADS calculations.

III. PERFORMANCE EVALUATIONS

We evaluated our FADS algorithms through simulation experiments that assessed estimation accuracy and consistency as well as computing speed for a range of (n, p, q) settings.

A. Experimental setup

We simulated 100 datasets for each $(n, p) \in \{(300, 30), (1000, 100)\}$ and $q \in \{3, 5\}$. Our strategy for each dataset was to set the diagonal elements of Ψ as i.i.d. $\mathcal{U}(0.2, 0.8)$ and entries in Λ as i.i.d. $\mathcal{N}(0, 1)$ pseudo-random deviates. Entries of μ were simulated independently from $\mathcal{N}(0, 1)$ and l_2 -normalized. A separate evaluation – to mimic the $p \gg n$ setting of the application in Section I-A4 – used 100 simulated datasets with $(p, q) = (5123, 12)$ and $n \in \{380, 500\}$, with the true Ψ, Λ, μ set to the ML estimates obtained upon fitting FADS-P to the TCGA dataset. In all cases, we stopped FADS-P and FADS-D when the improvement in the observed log-likelihood did not exceed 10^{-4} and $\|\nabla Q_P\|_\infty < \sqrt{\epsilon_0}$, where $\epsilon_0 \approx 2.2 \times 10^{-16}$ is the machine tolerance, or if the number of iterations exceeded 10^4 . For each simulated dataset, we fitted models with $k = 1, 2, \dots, 2q$ factors and chose the number of factors using eBIC. All experiments were run on a workstation with Intel E5-2640 v3 CPU clocked @2.60 GHz and 64GB RAM.

B. Results

In our experiments, eBIC always correctly picked q . Since factor loadings and uniquenesses are better interpreted on the correlation scale [26], we considered the parameters $\Lambda_{\mathfrak{R}} = \text{diag}(\sigma)^{-1/2} \Lambda$, $\Psi_{\mathfrak{R}} = \text{diag}(\sigma)^{-1} \Psi$, $\Upsilon_{\mathfrak{R}} = \Lambda_{\mathfrak{R}} \Lambda_{\mathfrak{R}}^\top$ and $\mathfrak{R} = \Upsilon_{\mathfrak{R}} + \Psi_{\mathfrak{R}}$, where σ is the vector of marginal standard deviations in Σ . We compared the FADS-D and FADS-P estimates using the relative Frobenius distances: $d_{\mathfrak{R}} = \|\widehat{\mathfrak{R}} - \mathfrak{R}\|_F / \|\mathfrak{R}\|_F$, $d_{\Upsilon_{\mathfrak{R}}} = \|\widehat{\Upsilon}_{\mathfrak{R}} - \Upsilon_{\mathfrak{R}}\|_F / \|\Upsilon_{\mathfrak{R}}\|_F$, $d_{\Psi_{\mathfrak{R}}} = \|\widehat{\Psi}_{\mathfrak{R}} - \Psi_{\mathfrak{R}}\|_F / \|\Psi_{\mathfrak{R}}\|_F$, $d_{\hat{\mu}} = \|\widehat{\mu} - \mu\|_F / \|\mu\|_F = \|\widehat{\mu} - \mu\|_F$, $d_{\hat{\sigma}} = \|\widehat{\sigma} - \sigma\|_F / \|\sigma\|_F$, and $d_{\hat{\Gamma}} = \|\widehat{\Gamma} - \Gamma\|_F / \|\Gamma\|_F$, where $\|\mathbf{A}\|_F = \text{Tr } \mathbf{A}^\top \mathbf{A}$ denotes the Frobenius norm of any matrix \mathbf{A} , $\widehat{\Gamma} = \widehat{\Lambda}^\top \widehat{\Psi}^{-1} \widehat{\Lambda}$, $\mathfrak{R} = \Upsilon_{\mathfrak{R}} + \Psi_{\mathfrak{R}}$ with $\widehat{\Upsilon}_{\mathfrak{R}} = \widehat{\Lambda}_{\mathfrak{R}} \widehat{\Lambda}_{\mathfrak{R}}^\top$ are the ML estimates.

Fig. 2a presents the relative speed of FADS-P to FADS-D for the randomly simulated cases – see Section S2.2 for average CPU time. (Our reported compute times include the common initialization time for both algorithms.) For $(n, p) \in \{(300, 30), (1000, 100)\}$, FADS-P was faster than FADS-D, with maximum speedup occurring at true q . FADS-P also generally needed far fewer iterations than FADS-D to converge. In particular, FADS-D did not converge even within 10^4 iterations for four $(n, p, q) = (1000, 100, 5)$ cases. In contrast, FADS-P always converged even though it required more iterations in the over-fitted models than when the fitted q did not exceed the true q (Section S2.1). Therefore, the speedup of FADS-P relative to FADS-D was slightly underestimated because of the censored reports from FADS-D.

For the data-driven cases where $n \ll p$, FADS-D never converged within 10^4 iterations, but FADS-P always converged successfully. So we only report FADS-P estimates for $n \ll p$, and calculate and compare estimation accuracy of FADS-D and FADS-P for the $n > p$ cases where both of them converged. (The four $n > p$ cases where FADS-D did not converge had terminating results that were not significantly different in estimation accuracy from those from FADS-P.) FADS-P and FADS-D yielded identical values of $\widehat{\mathfrak{R}}, \widehat{\Gamma}, \widehat{\Upsilon}_{\mathfrak{R}}$ and $\widehat{\Psi}_{\mathfrak{R}}$ under the best-fitted models, so the relative estimation errors (Figure 2b) were also identical. The relative errors for μ and σ were also similar for FADS-P and FADS-D. With $n \ll p$, the relative errors of FADS-P estimates decreased with increasing sample size (Table I and Figs. 2b and S1).

The results of our experiments show that FADS-P and FADS-D (when it converges) can, along with the use of eBIC, accurately recover factor structures underlying our PN model. Overall, FADS-P provides faster and more reliable estimates, so we use it in our applications.

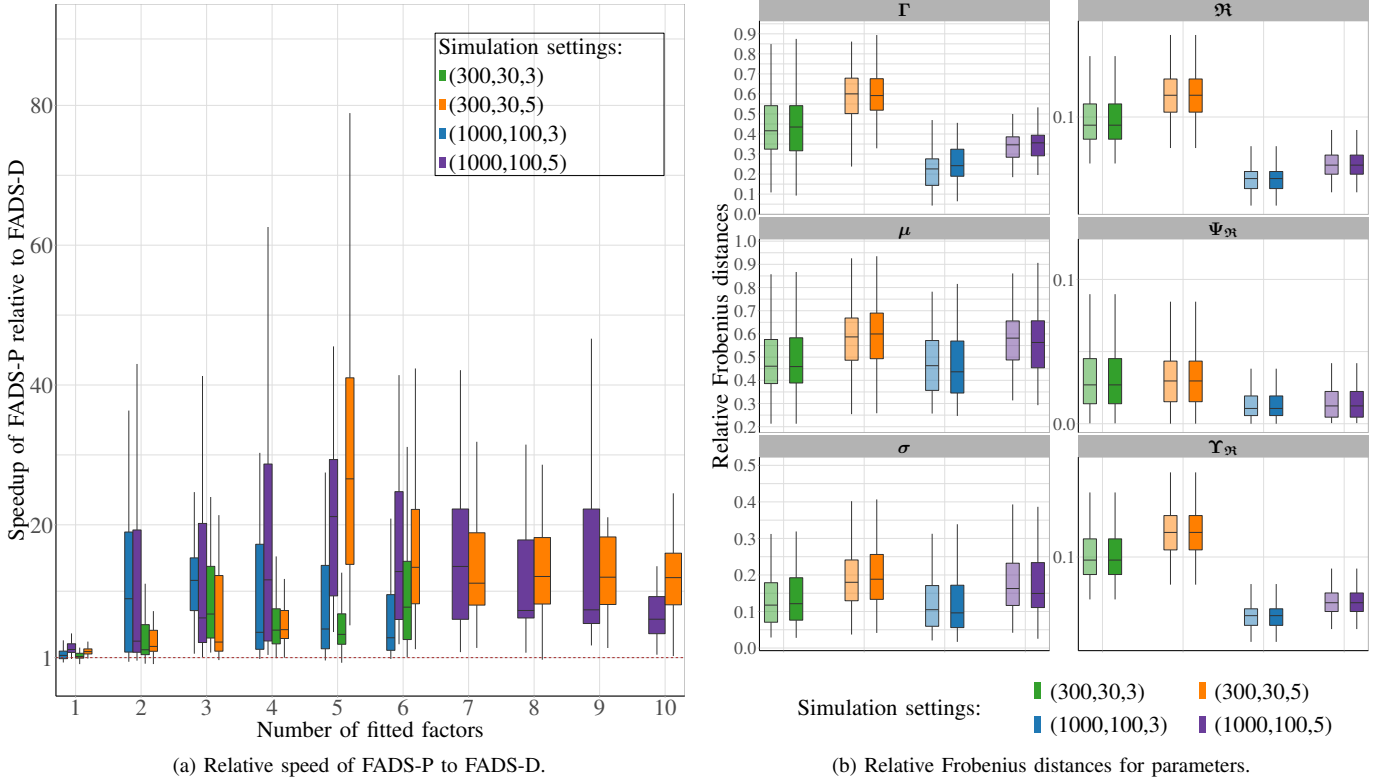


Fig. 2: (a) Computational speed of FADS-P relative to FADS-D. (b) Estimation accuracy of FADS-D (lighter shades) and FADS-P (darker shades). The experimental settings (n, p, q) are in parentheses.

TABLE I: Average relative Frobenius distances of FADS-P for the $p \gg n$ experiments.

(n, p, q)	\mathfrak{R}	Γ	$\Upsilon_{\mathfrak{R}}$	$\Psi_{\mathfrak{R}}$	μ	σ
(380,5123,12)	0.020	0.330	0.020	0.186	1.191	0.693
(500,5123,12)	0.020	0.326	0.020	0.184	1.188	0.689

IV. REAL DATA APPLICATIONS

We applied FADS-P to the four datasets of Section I-A. For each dataset, we first discuss how its processing places the observations on the unit sphere and then fit, analyze and interpret our factor models. We also provide diagnostic checks to verify the preference for our PN factor model over the existing (Langevin/Fisher-von Mises) model. The Langevin distribution has hitherto been the only one routinely used to directly model observations on unit spheres of as high dimensions as our applications, so our diagnostic is in the form of a hypothesis test, where the null hypothesis is that $\mathbf{X}_1, \mathbf{X}_2, \dots, \mathbf{X}_n$ are i.i.d. realizations from the p -variate Langevin distribution $\mathcal{L}_p(\kappa, \boldsymbol{\nu})$ with mean direction vector $\boldsymbol{\nu}$ and concentration parameter κ . The alternative hypothesis specifies each $\mathbf{X}_i \sim \mathcal{PN}_p(\boldsymbol{\mu}, \boldsymbol{\Lambda}\boldsymbol{\Lambda}^\top + \boldsymbol{\Psi})$, where $\boldsymbol{\mu}^\top \boldsymbol{\mu} = 1$, $\boldsymbol{\Lambda}$ is a $p \times q$ matrix and $\boldsymbol{\Psi}$ is a diagonal matrix. Our test statistic is the difference in maximized log-likelihood ($V = \ell_a - \ell_0$) of the data using the $\mathcal{L}_p(\kappa, \boldsymbol{\nu})$ and $\mathcal{PN}_p(\boldsymbol{\mu}, \boldsymbol{\Lambda}\boldsymbol{\Lambda}^\top + \boldsymbol{\Psi})$ models the optimal q selected from the data using eBIC. We use [68]’s exact Monte Carlo method to calculate the p -value of our test statistic in each application. Under this framework, the alternative model is favored by a large test statistic V_0 computed from the observed data compared with the values V_1, V_2, \dots, V_M , test statistics obtained from the M Monte Carlo samples generated under the (null) $\mathcal{L}_p(\kappa, \boldsymbol{\nu})$ distribution with parameters estimated from fitting the $\mathcal{L}_p(\kappa, \boldsymbol{\nu})$ model to the original data. We fit both the $\mathcal{L}_p(\kappa, \boldsymbol{\nu})$ and $\mathcal{PN}_p(\boldsymbol{\mu}, \boldsymbol{\Lambda}\boldsymbol{\Lambda}^\top + \boldsymbol{\Psi})$ models to the i th Monte Carlo sample, obtaining the maximized likelihood values, $\ell_0^{(i)}$ and $\ell_a^{(i)}$, and $V_i = \ell_a^{(i)} - \ell_0^{(i)}$. The exact Monte Carlo p -value was the rank of V_0 in $\{V_0, V_1, V_2, \dots, V_M\}$ divided by $M + 1$. The p -value calculation may be accelerated [69], but this speedup was not needed here.

A. Characterizing major themes underlying the #MeToo tweets

1) *Data collection and preprocessing*: We collected all 43,247 original tweets (excluding so-called re-tweets) in English that contained the #MeToo hashtag between December 03, 2018 at 02:06:15 (UTC) and December 13, 2018 at 01:36:20 (UTC). These tweets originally had 1,165,762 unique words. Standard text preprocessing put the dataset through (1) unitization and tokenization, (2) standardization and cleansing, (3) stop word removal, and (4) stemming and lemmatization [70]. In addition,

infrequently-occurring words (appearing in less than 0.25% of tweets) were removed from the lexicon, following [10]. We also removed one-word tweets because they contribute no information on relationships between terms. The resulting collection had $n = 31,385$ unique tweets and $p = 721$ unique words (see Section S3.1). (Henceforth, we use tweets to refer to this reduced dataset.) We applied the commonly used term frequency-inverse document frequency (*tf-idf*) weighting [70] to modulate the relative frequency of each word by tweet length. This procedure weighted d_{ij} , or the raw frequency of the j th word, in the i th tweet by $\log(n/d_{.j})$ where $d_{.j} = \sum_{i=1}^n d_{ij}$ is the number of tweets with the j th word. We therefore have a *tf-idf* weighted document-term matrix (DTM). Each tweet vector was then l_2 -normalized, placing it on the unit sphere. The l_2 -normalization mitigates the effect of differing tweet lengths [11] and also allows for the use of cosine similarity that performs better than the Euclidean distance metric on sparse text data [71]. The l_2 -normalized data $\mathbf{X}_1, \mathbf{X}_2, \dots, \mathbf{X}_n$ is our dataset for analysis.

2) *Results and analysis*: We applied FADS-P, with $q = 0, 1, 2, \dots, 15$, to the processed dataset of Section IV-A1. The eBIC chose the eight-factor model, which was significantly preferred over the Langevin model (p -value < 0.001). Fig. 3a displays the estimated uniquenesses for the fitted model, and is similar to the relative frequency of words contributing to the main discussion topics in the #MeToo movement during the given time period. We analyzed the eight factor loadings from the fitted model using quartimax rotation that simplifies interpretation by minimizing both the number of heavily loaded features on each factor and the number of factors needed to explain a feature [45]. Figs. 3b–i provide *word clouds* of the eight factor loadings, ordered by the proportion of variance in Σ explained. The word clouds provide insight into the dominant words that characterize each factor and help describe the variability in the #MeToo tweets. We now discuss and interpret the eight factors.

The first, fourth and sixth factors pertain to words appearing in tweets discussing different aspects of sexual harassment in the workplace. For instance, the first factor is dominated by words that appear in tweets discussing the December 3, 2018 Bloomberg article [72] titled “Wall Street Rule For The #MeToo Era: Avoid Women At All Cost” that outlines exclusionary strategies reportedly adopted by male Wall Street employees to avoid allegations in the #MeToo era, but that simultaneously raise obstacles for professional women and exacerbate gender segregation. We notice similar trends in the sixth factor that heavily weights words appearing in tweets discussing dilemmas faced by women in the workplace as their male colleagues limit professional contact (*e.g.*, by excluding them from dinner outings, solo meetings, sitting together while flying) to avoid accusations of professional sexual misconduct. So, though the words and topics are similar in these two factors, the first factor is focused on the Bloomberg article and avoidance strategies adopted by men on Wall Street while the sixth factor relates to avoidance issues in the general workplace. The related fourth factor is a contrast between the dominant terms “wall” and “street” on one hand and “cost”, “avoid”, “era”, “rule” and “women” on the other. Tweets with these words are generally about the December 5, 2018 Bloomberg article “NYC officials blast Wall Street’s ice-out of women in wake of #MeToo” [73] in response to the article associated with the first factor. These tweets mainly criticise Wall Street men’s reported strategy of avoiding women in the workplace, and instead school them on appropriate behaviours in a professional setting.

The second factor prominently loads words that are in tweets reacting to the cancellation by several radio stations, in the last week of November 2018, of the 1940s classic Christmas song “Baby It’s Cold Outside”, in response to listener complaints about its lyrics describing inappropriate and manipulative male behaviors toward women. Tweets with these words generally support the ban, though some others argue that the song was written in a different era.

The third factor primarily weights words conveying sexual assault, harassment, abuse and violence, and, to a lesser extent, “women”, “allege”, “survive” and “workplace”. We interpret this factor to reflect the main objectives of the #MeToo movement to expose sexual assault and harassment by men in power, especially in the workplace, and to provide support to survivors.

The remaining factors relate to politics and movements. The fifth factor has terms related to politics or policies, mostly appearing in tweets discussing the just concluded 2018 midterm elections in the United States, where female voters, female candidates and the #MeToo movement were generally viewed to have played a major role. The seventh factor is dominated by words that are in tweets related to movements for social justice and reform. Examples are tweets related to gender discrimination and harassment issues across generations and professions (farm workers, veterans, indigenous people, etc) or discussions on socio-political matters or allied movements like “Black Lives Matter” or “March for our Lives”, where millennials have been quite vocal and active. Conversely, the eighth factor is overwhelmingly weighted by words related to right-wing, misogynistic, white supremacist and conspiracy theory-based groups (#MAGA, QAnon, #Blexit, #MenToo, Men Going Their Own Way, etc) and their views on #MeToo, “Black Lives Matter” and other anti-fascist and social justice movements.

Z. Zhu has asked why we do not simply fit a (generative) Gaussian factor model to the tweets dataset before l_2 -normalization. The reason for not doing so is that the unnormalized tweet vectors cannot be assumed to all come from the same normal distribution. The processed tweets, after routine l_2 -normalization, are assumed to be i.i.d. from a PN factor model. The only other currently realistic model for such data is the Langevin distribution, but the hypothesis test reported on earlier fit our projected PN factor model significantly better than the Langevin model for this dataset. Our fitted model had eight factors that, upon quartimax rotation, provided insight into the main contributors of variability in the tweets.

B. Characterizing the pre-teen brain at rest

1) *Data preprocessing*: The data are from resting-state measurements [74] of 33 typically developing children between 8 and 12 years of age. Here, participants were instructed to relax and fixate on a crosshair while fMRI scans were acquired over

seven minutes, at intervals of 2.5s. The first 30s of data were discarded to let the scanner magnetization achieve a steady state, yielding 156 time points. For each registered, motion-corrected dataset, the AFNI software package [75], [76] used standard preprocessing techniques to regress out nuisance parameters. The residual time series for each subject at each of 75,589 in-brain voxels was normalized by its respective temporal mean and standard deviation [77], resulting in normalized time series on the surface of a 156-dimensional sphere. The normalized time series at each voxel were then summarized over the 33 pre-teens as the mean direction time series vector at each voxel. At this stage, we have a dataset D of $n = 75,589$ 156-dimensional observations on the unit sphere. However, regression (in this case, of the nuisance parameters) yields a singular matrix of residuals, so D is projected to a 69-dimensional space by means of a matrix of orthogonal rows spanning the null space of the regression hat matrix. (Any lower-dimensional orthogonal projection of a unit norm vector is also a unit norm vector in lower dimensional space if the projection vector is orthogonal to the null space of the vector being projected.) We thus have a dataset on the 69-dimensional unit sphere of $n = 75,589$ observations.

2) *Results and analysis*: FADS-P with eBIC chose the 2-factor model from among $q = 0, 1, 2, \dots, 10$. The PN factor model fit the data significantly better (p -value < 0.001) than its Langevin cousin. We backprojected the factor loadings to the original 156-dimensional space and used oblimin rotation for interpretable results that we now discuss.

Fig. 4a displays the time series of the oblimin-rotated factor loadings in 156-dimensional space, while Figs. 4b,c plot the

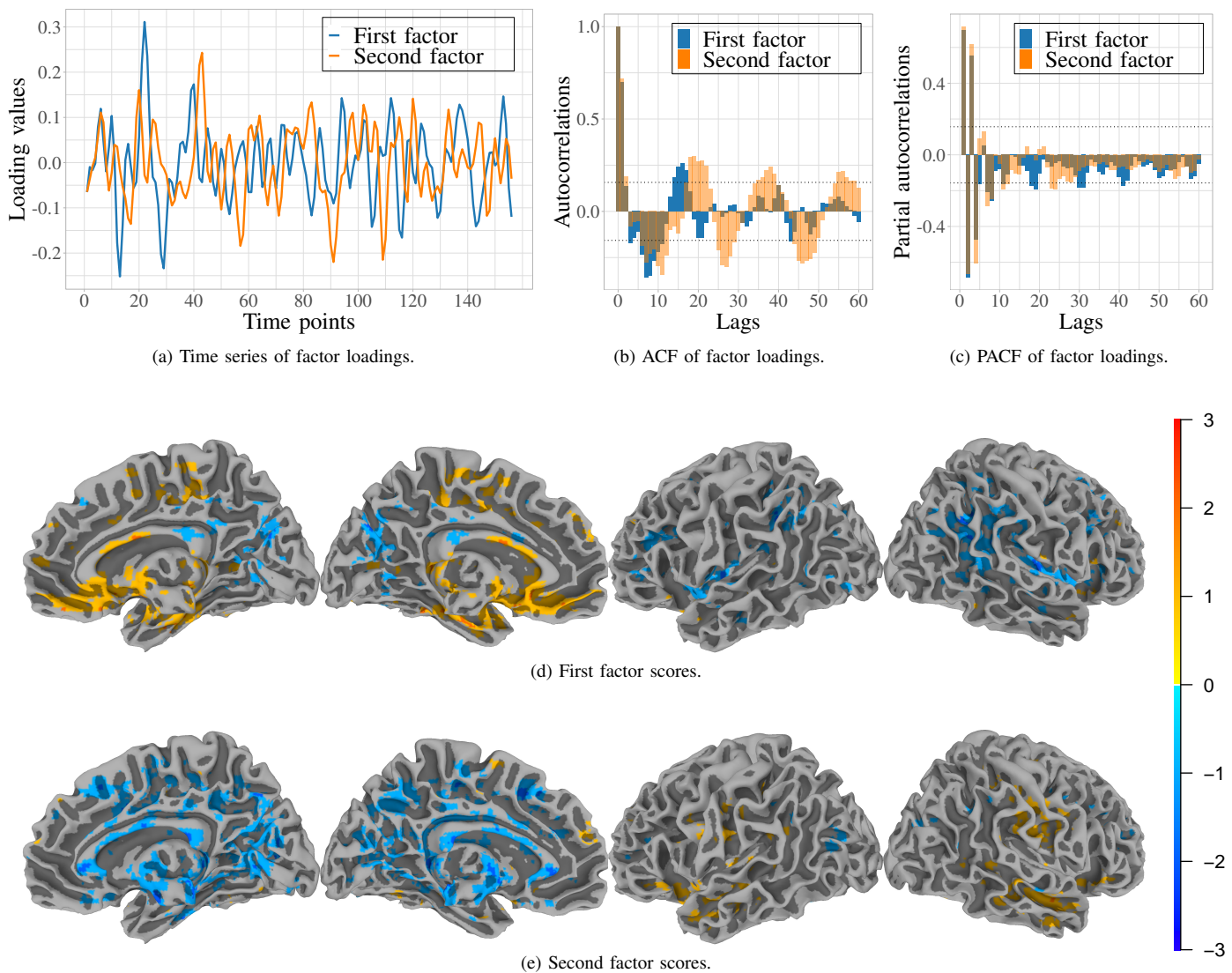


Fig. 4: Fitted factor loadings (a) time series, (b) ACF and (c) PACF of the pre-teen brain at rest show distinct characteristics. (d,e) The two predicted factor scores distribute to interpretable regions.

auto-correlation function (ACF) and partial ACF (PACF) along with 95% confidence intervals (broken lines). The first factor loadings show larger amplitude fluctuations between the tenth and fortieth time points than elsewhere. The second factor loadings fluctuate more frequently than the first, with a clearer seasonal pattern spanning approximately 15 time-points (37.5s)

in both the time series (Fig. 4a) and the ACF (Fig. 4b). The large spikes in the first few lags of the ACF for both factor loadings, followed by a cycle of decreasing (in magnitude) alternating negative and positive correlations, indicate a higher-order autoregression structure and a strong long-term seasonal component for the second factor loading. The PACF (Fig. 4c) also suggests presence of moving average terms, long-term dependencies and non-stationary components in both factor loadings. In summary, it appears that the variability over time of the in-brain voxels of the pre-teen brain at rest can be summarized in terms of two temporal components, both nonstationary and periodic, but one having longer-range dependence than the other. We now discuss the factor scores.

Figs. 4d,e provide voxel-wise displays of the two factor scores estimated as per Section II-D. The first factor scores are high in magnitude in the visual and sensory cortex, in areas of emotional and higher mental function (concentration, planning, judgment, emotional expression, creativity and inhibition) and in the motor function areas of the cerebellum that coordinate movement and balance. The second factor scores have non-negligible values in areas of the cerebral cortex involving visual, higher mental function, sensory association, olfactory and motor functions that initiate and orient the voluntary movement of muscles and the eye [78]. We see that the factor scores represent fairly functionally distinctive brain regions.

C. Handwritten digits

1) *Preprocessing*: As per Section I-A3, the dataset is of 70,000 784-pixel bitmap images. Fig. 5a displays 20 random specimens of each digit and shows variation in handwriting between (and within) digits. It is this variability that we want to characterize by our PN factor model. We removed pixels with the same value across all coordinates because they contribute no information on variability. Further, because of the discretized (bitmapped) values in the dataset, we jittered each of them by adding i.i.d. $\mathcal{N}(0, 0.1^2)$ pseudo-random deviates. The jittered images are essentially indistinguishable from the originals (Fig. S6) and were l_2 -normalized for use in our analysis.

2) *Results and Analysis*: The PN factor model was fit using FADS-P for $q = 0, 1, \dots, 15$: eBIC chose the 12-factor model that was found to fit the data significantly better (p -value < 0.001) than the Langevin. The factor loadings after quartimax rotation are displayed, in decreasing order of their contribution to the variance, in Fig. 5b (first column) – dropped pixels were set to zero for the factor loadings. For interpretability, we also used absolute correlation to assign each handwritten digit to its closest factor loading. Fig. 5b displays the relative-frequency-weighted mean of the assigned images for each factor-digit combination. We now discuss and interpret the factors.

The first factor in Fig. 5b (upper left) is largely an overall contrast between foreground and background pixels over all the digits, and consequently is strongly correlated with samples from each digit. The remaining 11 factor loadings are contrasts between different sets of pixels in the imaging regions. Indeed, each of them are correlated with different kinds of digits (see rows, and caption of Fig. 5b). For example, the second factor loading has high association primarily with “4” and “9” and to a lesser extent “6”, “7” and “0”. Images having high correlations with this factor loading have high values at many of the same pixel locations. Also, the 12th factor loading is primarily associated with large handwritten “7”s spanning the entire image. Some digits, such as “2” and “6”, are strongly associated with more factor loadings than others, probably because there are more handwriting styles (in terms of pixels used) for these digits. D. M. Ommen has pointed out that the third and eleventh factors are, strikingly, largely associated with upright-written digits, potentially indicating left-handed writers. (The MNIST dataset does not have information on handedness, so we are unable to verify this conjecture.)

D. Nettleton has asked about using traditional Gaussian factor analysis on this dataset, that is, essentially ignoring the constraints imposed by the digitization of a bitmap image. Doing so yielded poor results, unlike FADS that not only accounts for the imaging data acquisition process but also identified interpretable factors that capture the variability in handwriting styles both between and within digits. We remark that our methodology has not accounted for spatial context or pixel neighborhood. Incorporating these aspects may improve our results further.

D. TCGA dataset

1) *Data collection and preprocessing*: We use an mRNA sequence (RNA-seq) dataset comprised of 775 primary breast cancer (BC) tumors from the TCGA effort [79], prepared and released in the Bioconductor package `curatedTCGAData` [80]. RNA-seq leverages high-throughput next-generation sequencing technology [81] to examine the presence and quantity of mRNA from each gene in a biological sample by sequencing random deoxyribonucleic acid fragments derived from the sampled mRNA [82]. During data preparation, the sampled sequence fragments were mapped to 20,502 genes, producing a count of fragments for each gene. Since the total number of fragments sequenced (coverage) is not biologically meaningful, we scaled the counts in each experiment to sum to unity, and then screened out low expression genes, by discarding genes with mean scaled expressions below the third quartile, producing our dataset on 5,123 genes. After rescaling the 5,123 surviving gene proportions to sum to unity in each of the 775 experiments, we applied a square root transformation to place the compositional data on the unit sphere, as in [24].



Fig. 5: MNIST digits: (a) sample and (b) results. In (b), the first column has the factor loadings, while the rest have the weighted mean of the digits most correlated with the loadings of each factor. These displays show “0” as primarily related to the 4th and 11th factor loadings, “1” with the 5th, 8th, and 10th factors, “2” with the 4th and 6th–9th factors, “3” with the 3rd and 4th factors, “4” with the 2nd and 6th factors, “5” with the 3rd and 10th factors, “6” with the 2nd, 3rd, 7th, 9th and 11th factors, “7” with the 2nd, 5th, 6th, and 12th factors, “8” with the 3rd and 4th factors, and “9” with the 2nd, 5th, and 6th factors.

2) *Results and analysis*: FADS with eBIC selected a 12-factor model when fitting up to 15 factors. The first eight of these factors explained 95% of the variation in the data. This model also significantly (p -value < 0.001) out-performed the Langevin model in fitting the processed data. We used quartimax rotation for further analysis. To determine if any factor could be prognostic, we fitted the Cox proportional-hazards model [83] to the survival time of the 775 observations using each factor score in turn as the predictor. A likelihood ratio test indicated significant association of the sixth factor with survival (Holm’s corrected p -value of 0.005). Fig. 6a displays survival curves with the 95% confidence intervals, which are estimated using the Kaplan–Meier method [84], and obtained after thresholding on the median value (1.09925) of the sixth factor scores. The two survival curves are significantly different (p -value of 0.00069 via a logrank test [85]). Further, high values of the sixth factor correspond to increased survival, especially between years 2–8.

The sixth factor can be associated with genes to identify possible prognostic biomarkers or biological processes to hypothesize a mechanism for altered survival. In particular, it is common to identify the biological processes associated with gene-level statistics using gene set enrichment analysis (GSEA) [86]. We performed GSEA using the sixth factor loadings, on the correlation scale, as the gene-level statistic and an enrichment p -value was calculated for each of the 50 hallmark gene sets in the MSigDB collections, version 5 [87]. GSEA found the sixth factor enriched for 13 of the 50 hallmark gene sets with false discovery rate (FDR) adjusted p -values < 0.05 . Figure 6b presents the normalized enrichment scores (NES) and FDR-adjusted p -values of these thirteen selected gene sets.

We examine the five gene sets with FDR-adjusted p -values below 10^{-8} , comparing our findings to the literature. The INTERFERON_GAMMA_RESPONSE and INTERFERON_ALPHA_RESPONSE gene sets are immunity-related and substantially overlapped hallmark gene sets (Jaccard index 0.33). Though the role of the immune response in BC is far from clear [88], the constellation of genes activated in response to the interferon- γ cell-signaling cytokine have recently been associated with poor prognosis in another cohort of BC patients [89]. The top three loaded genes in *both* gene sets are IFI27, ISG15, and RSAD2.

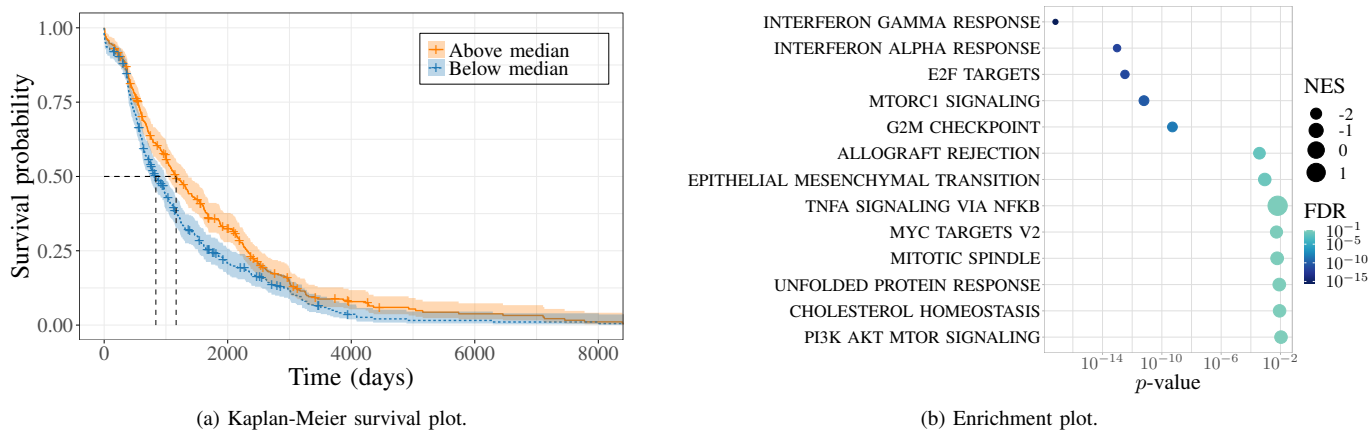


Fig. 6: (a) Kaplan-Meier survival plot split by median value of the sixth factor. Orange cases are above and blue are below the median. The horizontal and vertical dashed lines indicate the median survival times for the two groups. (b) Enrichment plot. Gene sets are labeled on y-axis.

IFI27 physically associates with estrogen receptor α , an important mediator of proliferation in BC [90], ISG15 modifies other proteins through ISGylation and correlates with lymphovascular invasion and poor prognosis [91], [92], and RSAD2, known to inhibit virus replication [93], associates with tumor stage and lymph node metastases [94]. The E2F_TARGETS and G2M_CHECKPOINT gene sets are involved in cell proliferation, a commonly upregulated function in tumor samples [95]. E2F transcription factors participate in cell cycle control, and several have recently been associated with BC prognosis [96], while the entire G2M_CHECKPOINT hallmark gene set has been deemed a prognostic biomarker of metastasis in one type of BC [97]. Transcription factor MYBL2 is the most (negatively) loaded gene on the sixth factor in *both* gene sets, while TOP2A is the second most (negatively) loaded gene among E2F targets and the third most (negatively) loaded G2M checkpoint gene. MYBL2 directly targets several kinesin motor proteins that are correlated with poor BC prognosis [98]. TOP2A is a DNA topoisomerase whose expression has been correlated with poor BC prognosis [95], [99]. In fact, it is a direct target of some chemotherapies, including a trial where its expression was successfully used to guide treatment [100]. The gene set MTORC1_SIGNALING consists of genes upregulated through activation of MTORC1, a protein complex responsible for protein synthesis that has also been targeted by chemotherapeutic agents for BC [101]. MTORC1 appears frequently in the BC literature as several prognostic markers are in MTORC1-related gene sets [102], [103], [104], [105]. Here, SQLE is the most (negatively) loaded gene on the MTORC1 gene set and the second most (negatively) loaded gene on the G2M gene set. It is an enzyme involved in cholesterol synthesis, with an impact on proliferation, that has been associated with poor prognosis [106], [107]. Thus, FADS finds a single, highly interpretable, apparently proliferation-related, axis of variation significantly associated with BC survival.

V. DISCUSSION

This paper develops methodology for exploratory factor analysis of data on a sphere, with a view to explaining the variability in the coordinates in terms of a few underlying (latent) factors. Such datasets arise in applications involving text documents, time series image volumes of the brain, digitized images, or compositional gene expression data, that we investigate in this paper. Our approach uses the PN distribution [4] which is the distribution of a normalized $\mathcal{N}_p(\boldsymbol{\mu}, \boldsymbol{\Sigma})$ random vector, with the restriction that $\boldsymbol{\mu} \in \mathcal{S}_{p-1}$ for identifiability. Our factor model is introduced through a decomposition of the generative MVN model. We develop computationally fast estimation methods for the parameters using two versions of the AECM algorithm. The first, called FADS-D, uses the latent factors and lengths of the random vectors of our generative model as the missing variables, while the second approach, called FADS-P, profiles out the latent factors in the generative model. We also provided uncertainty estimators for our models. Our methods are implemented in the developmental version of our `fad` package in R [108] that is available at <https://github.com/somakd/fad>. Simulation results show fast and excellent performance, especially of FADS-P with the number of factors well-estimated using eBIC. Analysis of datasets from four motivating applications provided interpretable insights into the underlying mechanisms governing variability in each case.

There are a number of points that could benefit from further attention. For instance, our PN factor model (and indeed the MVN factor model itself) could benefit from results on consistency of the eBIC. Further, our model could also be used in regression and classification settings, replacing, for instance, the Fisher distribution, in the development of the spherical regression model of [109], with appropriate modifications. Such an approach would allow us to characterize resting state brains in autistic and typically developing children, for example. Other extensions to be investigated include Bayesian methods for estimation, as well as including sparsity structures on $\mathbf{\Lambda}$. It may also be of interest to incorporate the PN model in settings

that involve a combination of p linear variables and q variables on S_{q-1} . From an applications perspective, we may also be interested in using factor scores in genome-wide association studies to account for population structure. Therefore, we see that there are many directions for further investigation.

ACKNOWLEDGMENTS

The research was supported in part by the United States Department of Agriculture (USDA)/National Institute of Food and Agriculture (NIFA), Hatch projects IOW03617 and IOW03717. The content of this paper however is solely the responsibility of the authors and does not represent the official views of the USDA.

REFERENCES

- [1] G. S. Watson, *Statistics on Spheres*, ser. University of Arkansas Lecture Notes in the Mathematical Sciences. Wiley Interscience, 1983.
- [2] N. Fisher, T. Lewis, and B. Embleton, *Statistical Analysis of Spherical Data*. Cambridge University Press, 1993.
- [3] S. R. Jammalamadaka and A. SenGupta, *Topics in Circular Statistics*. World Scientific, 2001.
- [4] K. V. Mardia and P. E. Jupp, *Directional Statistics*. New York: Wiley, 2000.
- [5] R. von Mises, "über die "ganzzahligkeit" der atomgewichte und verwandte fragen," *Physikalische Zeitung*, vol. 19, pp. 490–500, 1918.
- [6] R. A. Fisher, "Dispersion on a sphere," *Proc. R. Soc. Lond. A*, vol. 217, pp. 295–305, 1953.
- [7] A. SenGupta and R. Maitra, "On best equivariance and admissibility of simultaneous MLE for mean direction vectors of several Langevin distributions," *Annals of the Institute of Statistical Mathematics*, vol. 50, no. 4, pp. 715–27, 1998.
- [8] G. Salton and C. Buckley, "Term-weighting approaches in automatic text retrieval," *Information Processing and Management*, vol. 27, no. 5, pp. 513–523, 1988.
- [9] T. G. Kolda, "Limited-memory matrix methods with applications," Ph.D. dissertation, The Applied Mathematics Program, University of Maryland, College Park, Maryland, 1997.
- [10] I. S. Dhillon and D. S. Modha, "Concept decompositions for large sparse text data using clustering," *Machine Learning*, vol. 42, pp. 143–175, 2001.
- [11] A. Singhal, C. Buckley, M. Mitra, and G. Salton, "Pivoted document length normalization," in *ACM SIGIR'96*, 1996, pp. 21–29.
- [12] A. Banerjee, I. S. Dhillon, J. Ghosh, and S. Sra, "Clustering on the unit hypersphere using von Mises-Fisher distributions," *Journal of Machine Learning Research*, vol. 6, pp. 1345–1382, 2005.
- [13] B. Biswal, F. Z. Yetkin, V. M. Haughton, and J. S. Hyde, "Functional connectivity in the motor cortex of resting human brain using echo-planar MRI," *Magnetic Resonance in Medicine*, vol. 34, no. 4, pp. 537–541, 1995.
- [14] B. B. Biswal, "Resting state fMRI: A personal history," *NeuroImage*, vol. 62, no. 2, pp. 938 – 944, 2012.
- [15] J. W. Belliveau, D. N. Kennedy, R. C. McKinstry, B. R. Buchbinder, R. M. Weisskoff, M. S. Cohen, J. M. Vevea, T. J. Brady, and B. R. Rosen, "Functional mapping of the human visual cortex by magnetic resonance imaging," *Science*, vol. 254, pp. 716–719, 1991.
- [16] K. K. Kwong, J. W. Belliveau, D. A. Chesler, I. E. Goldberg, R. M. Weisskoff, B. P. Poncelet, D. N. Kennedy, B. E. Hoppel, M. S. Cohen, R. Turner, H.-M. Cheng, T. J. Brady, and B. R. Rosen, "Dynamic magnetic resonance imaging of human brain activity during primary sensory stimulation," *Proceedings of the National Academy of Sciences of the United States of America*, vol. 89, pp. 5675–5679, 1992.
- [17] P. A. Bandettini, A. Jesmanowicz, E. C. Wong, and J. S. Hyde, "Processing strategies for time-course data sets in functional mri of the human brain," *Magnetic Resonance in Medicine*, vol. 30, pp. 161–173, 1993.
- [18] M. A. Lindquist, "The statistical analysis of fMRI data," *Statistical Science*, vol. 23, no. 4, pp. 439–464, 2008.
- [19] N. A. Lazar, *The Statistical Analysis of Functional MRI Data*. Springer, 2008.
- [20] M. D. Fox, A. Z. Snyder, J. L. Vincent, M. Corbetta, D. C. Van Essen, and M. E. Raichle, "The human brain is intrinsically organized into dynamic, anticorrelated functional networks," *Proceedings of the National Academy of Sciences*, vol. 102, no. 27, pp. 9673–9678, 2005.
- [21] D. Cole, S. Smith, and C. Beckmann, "Advances and pitfalls in the analysis and interpretation of resting-state fMRI data," *Frontiers in Systems Neuroscience*, vol. 4, p. 8, 2010.
- [22] R. Maitra and I. P. Ramler, "A k -mean-directions algorithm for efficient clustering of data on a sphere," *Journal of Computational and Graphical Statistics*, vol. 19, no. 2, pp. 377–396, 2010.
- [23] Y. LeCun, C. Cortes, and C. J. C. Burges, "The mnist database," 2019. [Online]. Available: <http://yann.lecun.com/exdb/mnist/>
- [24] X. Dai and H.-G. Müller, "Principal component analysis for functional data on Riemannian manifolds and spheres," *Annals of Statistics*, vol. 46, no. 6B, pp. 3334–3361, 12 2018.
- [25] K. Bose and P. Chaudhari, *Unravelling Cancer Signaling Pathways: A Multidisciplinary Approach*. Springer, 2019.
- [26] K. V. Mardia, J. T. Kent, and J. M. Bibby, *Multivariate analysis*. New York: Academic Press, 1979.
- [27] J. Dortet-Bernadet and N. Wicker, "Model-based clustering on the unit sphere with an illustration using gene expression profiles," *Biostatistics*, vol. 9, no. 1, pp. 66–80, 2008.
- [28] C. Bingham, "An antipodally symmetric distribution on the sphere," *Annals of Statistics*, vol. 2, pp. 1201–1225, 1974.
- [29] J. T. Kent, "The Fisher–Bingham distribution on the sphere," *Journal of the Royal Statistical Society*, vol. 44, pp. 71–80, 1982.
- [30] I. Dryden, "Statistical analysis on high-dimensional spheres and shape spaces," *Annals of Statistics*, vol. 33, pp. 1643–1665, 09 2005.
- [31] B. Kim, S. Huckemann, J. Schulz, and S. Jung, "Small sphere distributions for directional data with application to medical imaging," *Scandinavian Journal of Statistics*, pp. 432–444, 05 2017.
- [32] F. Wang and A. E. Gelfand, "Directional data analysis under the general projected normal distribution," *Statistical Methodology*, vol. 10, pp. 113–127, 07 2013.
- [33] D. Hernandez-Stumpfhauser, F. Breidt, and M. Woerd, "The general projected normal distribution of arbitrary dimension: Modeling and Bayesian inference," *Bayesian Analysis*, vol. 12, pp. 113–133, 01 2016.
- [34] X. Meng and D. van Dyk, "The EM algorithm — an old folk-song sung to a fast new tune (with discussion)," *Journal of the Royal Statistical Society B*, vol. 59, pp. 511–567, 1997.
- [35] R. Varadhan and C. Roland, "Simple and globally convergent methods for accelerating the convergence of any em algorithm," *Scandinavian Journal of Statistics*, vol. 35, pp. 335–353, 06 2008.
- [36] J. Chen and Z. Chen, "Extended bayesian information criteria for model selection with large model spaces," *Biometrika*, vol. 95, no. 3, pp. 759–771, 2008.
- [37] T. M. Pukkila and C. R. Rao, "Pattern recognition based on scale invariant discriminant functions," *Information sciences*, vol. 45, no. 3, pp. 379–389, 1988.
- [38] P. J. Paine, S. Preston, M. Tsagris, and A. Wood, "An elliptically symmetric angular gaussian distribution," *Statistics and Computing*, vol. 28, pp. 689–697, 05 2018.
- [39] D. N. Lawley, "The estimation of factor loadings by the method of maximum likelihood," *Proceedings of the Royal Society of Edinburgh*, vol. 60, no. 1, p. 64–82, 1940.

- [40] K. G. Jöreskog, "Some contributions to maximum likelihood factor analysis," *ETS Research Bulletin Series*, no. 2, pp. 1–54, 1966.
- [41] D. N. Lawley, A. E. Maxwell, and A. Ernest, *Factor analysis as a statistical method*, 2nd ed. New York : American Elsevier Publishing Company, 1971.
- [42] T. W. Anderson, *An Introduction to multivariate statistical analysis*, ser. Wiley Series in Probability and Statistics. Wiley, 2003.
- [43] A. B. Owen and J. Wang, "Bi-cross-validation for factor analysis," *Statistical Science*, vol. 31, pp. 119–139, 03 2015.
- [44] F. Dai, S. Dutta, and R. Maitra, "A matrix-free likelihood method for exploratory factor analysis of high-dimensional gaussian data," *Journal of Computational and Graphical Statistics*, vol. 29, no. 3, pp. 675–680, 2020.
- [45] A. B. Costello and J. Osborne, "Best practices in exploratory factor analysis: Four recommendations for getting the most from your analysis," *Practical Assessment, Research and Evaluation*, vol. 10, pp. 1–9, 01 2005.
- [46] D. Rubin and D. Thayer, "Em algorithms for ml factor analysis," *Psychometrika*, vol. 47, pp. 69–76, 02 1982.
- [47] H. V. Henderson and S. R. Searle, "On deriving the inverse of a sum of matrices," *SIAM Review*, vol. 23, no. 1, pp. 53–60, 1981. [Online]. Available: <http://www.jstor.org/stable/2029838>
- [48] R. H. Byrd, J. N. P. Lu, and C. Zhu, "A limited memory algorithm for bound constrained optimization," *SIAM Journal on Scientific Computing*, vol. 16, pp. 1190–1208, 1995.
- [49] R. Piessens, E. de Doncker-Kapenga, C. W. Überhuber, and D. K. Kahaner, *Quadpack: a subroutine package for automatic integration*. Springer-Verlag, 1983, vol. 1.
- [50] D. C. Sorensen, "Implicit application of polynomial filters in a k -step arnoldi method," *SIAM Journal on Matrix Analysis and Applications*, vol. 13, no. 1, pp. 357–385, 1992.
- [51] S. Dutta and D. Mondal, "An h-likelihood method for spatial mixed linear model based on intrinsic autoregressions," *Journal of the Royal Statistical Society: Series B (Statistical Methodology)*, vol. 77, pp. 699–726, 09 2015.
- [52] J. H. Wilkinson, "The calculation of the eigenvectors of codiagonal matrices," *Computer Journal*, vol. 1, pp. 90–96, 02 1958.
- [53] R. Maitra, "Initializing partition-optimization algorithms," *IEEE/ACM Transactions on Computational Biology and Bioinformatics*, vol. 6, pp. 144–157, 2009.
- [54] —, "On the expectation-maximization algorithm for Rice-Rayleigh mixtures with application to estimating the noise parameter in magnitude MR datasets," *Sankhyā: The Indian Journal of Statistics, Series B*, vol. 75, no. 2, p. 293–318, 2013.
- [55] G. Schwarz, "Estimating the dimensions of a model," *Annals of Statistics*, vol. 6, pp. 461–464, 1978.
- [56] R. Argelaguet, B. Velten, D. Arnol, S. Dietrich, T. Zenz, J. C. Marioni, F. Buettner, W. Huber, and O. Stegle, "Multi-omics factor analysis—a framework for unsupervised integration of multi-omics data sets," *Molecular Systems Biology*, vol. 14, no. 6, p. e8124, 2018.
- [57] C. Meng, D. Helm, M. Frejno, and B. Kuster, "moCluster: identifying joint patterns across multiple omics data sets," *Journal of Proteome Research*, vol. 15, no. 3, pp. 755–765, 2016.
- [58] Q. Mo, R. Shen, C. Guo, M. Vannucci, K. S. Chan, and S. G. Hilsenbeck, "A fully bayesian latent variable model for integrative clustering analysis of multi-type omics data," *Biostatistics*, vol. 19, no. 1, pp. 71–86, 2018.
- [59] R. Shen, A. B. Olshen, and M. Ladanyi, "Integrative clustering of multiple genomic data types using a joint latent variable model with application to breast and lung cancer subtype analysis," *Bioinformatics*, vol. 25, no. 22, pp. 2906–2912, 2009.
- [60] D. Grün, A. Lyubimova, L. Kester, K. Wiebrands, O. Basak, N. Sasaki, H. Clevers, and A. Van Oudenaarden, "Single-cell messenger RNA sequencing reveals rare intestinal cell types," *Nature*, vol. 525, no. 7568, pp. 251–255, 2015.
- [61] W. Saelens, R. Cannoodt, H. Todorov, and Y. Saeys, "A comparison of single-cell trajectory inference methods," *Nature Biotechnology*, vol. 37, no. 5, pp. 547–554, 2019.
- [62] C. DiStefano, M. Zhu, and D. Mindrila, "Understanding and using factor scores: Considerations for the applied researcher," *Practical Assessment, Research, and Evaluation*, vol. 14, no. 1, p. 20, 2009.
- [63] N. Patterson, A. L. Price, and D. Reich, "Population structure and eigenanalysis," *PLoS Genetics*, vol. 2, no. 12, p. e190, 2006.
- [64] A. L. Price, N. J. Patterson, R. M. Plenge, M. E. Weinblatt, N. A. Shadick, and D. Reich, "Principal components analysis corrects for stratification in genome-wide association studies," *Nature Genetics*, vol. 38, no. 8, pp. 904–909, 2006.
- [65] J. Novembre and M. Stephens, "Interpreting principal component analyses of spatial population genetic variation," *Nature Genetics*, vol. 40, no. 5, pp. 646–649, 2008.
- [66] L. L. Thurstone, *The vectors of mind: Multiple-factor analysis for the isolation of primary traits*. University of Chicago Press, 1935.
- [67] T. A. Louis, "Finding the observed information matrix when using the EM algorithm," *Journal of the Royal Statistical Society, Series B (Methodological)*, vol. 44, no. 2, pp. 226–233, 1982.
- [68] G. A. Barnard, "Discussion of "the spectral analysis of point processes" by m. s. bartlett," *Journal of the Royal Statistical Society: Series B*, vol. 25, pp. 264–294, 1963.
- [69] J. Besag and P. Clifford, "Sequential Monte Carlo p-values," *Biometrika*, vol. 78, pp. 301–304, 1991.
- [70] M. Anandarajan, C. Hill, and T. Nolan, *Practical text analytics: Maximizing the value of text data*, 1st ed. Springer Publishing Company, Incorporated, 2018.
- [71] G. Lebanon, "Metric learning for text documents," *IEEE Transactions on Pattern Analysis and Machine Intelligence*, vol. 28, pp. 497–508, 05 2006.
- [72] G. Tan and K. Porzecanski, "Wall street rule for the #metoo era: Avoid women at all cost," *Bloomberg*, 12 2018.
- [73] —, "NYC officials blast Wall Street's ice-out of women in wake of #metoo," *Bloomberg*, 12 2018.
- [74] M. B. Nebel, S. Joel, J. Muschelli, A. Barber, B. Caffo, J. Pekar, and S. Mostofsky, "Disruption of functional organization within the primary motor cortex in children with autism," *Human Brain Mapping*, vol. 35, pp. 567–580, 02 2014.
- [75] R. W. Cox, "Afni: software for analysis and visualization of functional magnetic resonance neuroimages," *Computers and Biomedical research*, vol. 29, no. 3, pp. 162–173, 1996.
- [76] —, "AFNI: What a long strange trip it has been," *NeuroImage*, vol. 62, pp. 743–747, 2012.
- [77] C.-J. Chen and J.-L. Wang, "A new approach for functional connectivity via alignment of blood oxygen level-dependent signals," *Brain Connectivity*, vol. 9, no. 6, pp. 464–474, 2019.
- [78] K. Sukef, *Neuroanatomy: The Basics*, 2019. [Online]. Available: <https://www.dana.org/article/neuroanatomy-the-basics/>
- [79] J. N. Weinstein, E. A. Collisson, G. B. Mills, K. R. M. Shaw, B. A. Ozenberger, K. Ellrott, I. Shmulevich, C. Sander, and J. M. Stuart, "The cancer genome atlas pan-cancer analysis project," *Nature Genetics*, vol. 45, no. 1010, p. 1113–1120, 2013.
- [80] M. Ramos, *curatedTCGAData: Curated Data From The Cancer Genome Atlas (TCGA) as MultiAssayExperiment Objects*, 2020, r package version 1.10.0.
- [81] M. L. Metzker, "Sequencing technologies - the next generation," *Nature Review Genetics*, vol. 11, p. 31–46, 2010.
- [82] Z. Wang, M. Gerstein, and M. Snyder, "Rna-seq: A revolutionary tool for transcriptomics," *Nature reviews. Genetics*, vol. 10, pp. 57–63, 12 2008.
- [83] D. R. Cox, "Regression models and life-tables," *Journal of the Royal Statistical Society, Series B (Methodological)*, vol. 34, no. 2, pp. 187–220, 1972.
- [84] E. L. Kaplan and P. Meier, "Nonparametric estimation from incomplete observations," *Journal of the American Statistical Association*, vol. 53, no. 282, pp. 457–481, 1958.
- [85] N. Mantel, "Evaluation of survival data and two new rank order statistics arising in its consideration," *Cancer Chemotherapy Reports*, vol. 50, no. 3, pp. 163–170, 1966.

- [86] A. Subramanian, P. Tamayo, V. K. Mootha, S. Mukherjee, B. L. Ebert, M. A. Gillette, A. Paulovich, S. L. Pomeroy, and T. R. Golub, “Gene set enrichment analysis: a knowledge-based approach for interpreting genome-wide expression profiles.” *Proceedings of the National Academy of Sciences*, vol. 102, pp. 15 545–15 550, 10 2005.
- [87] A. Liberzon, C. Birger, H. Thorvaldsdóttir, M. Ghandi, J. P. Mesirov, and P. Tamayo, “The Molecular Signatures Database (MSigDB) hallmark gene set collection,” *Cell Systems*, vol. 1, no. 6, pp. 417–425, 12 2015.
- [88] M. E. Gatti-Mays, J. M. Balko, S. R. Gameiro, H. D. Bear, S. Prabhakaran, J. Fukui, M. L. Disis, R. Nanda, J. L. Gulley, K. Kalinsky, H. A. Sater, J. A. Sparano, D. Cescon, D. B. Page, H. McArthur, S. Adams, and E. A. Mittendorf, “If we build it they will come: Targeting the immune response to breast cancer,” *npj Breast Cancer*, vol. 5, no. 1, pp. 1–13, 10 2019.
- [89] A.-S. Heimes, F. Härtner, K. Almstedt, S. Krajnak, A. Lebrecht, M. J. Battista, K. Edlund, W. Brenner, A. Hasenburg, U. Sahin, M. Gehrmann, J. G. Hengstler, and M. Schmidt, “Prognostic significance of interferon- γ and its signaling pathway in early breast cancer depends on the molecular subtypes,” *International Journal of Molecular Sciences*, vol. 21, no. 1919, p. 7178, 1 2020.
- [90] M. G. Cervantes-Badillo, A. Paredes-Villa, V. Gómez-Romero, R. Cervantes-Roldán, L. E. Arias-Romero, O. Villamar-Cruz, M. González-Montiel, T. Barrios-García, A. J. Cabrera-Quintero, G. Rodríguez-Gómez, L. Cancino-Villeda, A. Zentella-Dehesa, and A. Le’on-Del-Río, “IFI27/ISG12 downregulates estrogen receptor α transactivation by facilitating its interaction with CRM1/XPO1 in breast cancer cells,” *Frontiers in Endocrinology*, vol. 11, p. 568375, 2020.
- [91] N. Bektas, E. Noetzel, J. Veeck, M. F. Press, G. Kristiansen, A. Naami, A. Hartmann, A. Dimmler, M. W. Beckmann, R. Knüchel, P. A. Fasching, and E. Dahl, “The ubiquitin-like molecule interferon-stimulated gene 15 (ISG15) is a potential prognostic marker in human breast cancer,” *Breast Cancer Research*, vol. 10, no. 4, p. R58, Jul 2008.
- [92] Y. A. Kariri, M. Alsaleem, C. Joseph, S. Alsaeed, A. Aljohani, S. Shiino, O. J. Mohammed, M. S. Toss, A. R. Green, and E. A. Rakha, “The prognostic significance of interferon-stimulated gene 15 (ISG15) in invasive breast cancer,” *Breast Cancer Research and Treatment*, vol. 185, no. 2, pp. 293–305, 1 2021.
- [93] E. E. Rivera-Serrano, A. S. Gizzi, J. J. Arnold, T. L. Grove, S. C. Almo, and C. E. Cameron, “Viperin reveals its true function,” *Annual Review of Virology*, vol. 7, no. 1, pp. 421–446, 9 2020.
- [94] J. Tang, Q. Yang, Q. Cui, D. Zhang, D. Kong, X. Liao, J. Ren, Y. Gong, and G. Wu, “Weighted gene correlation network analysis identifies RSAD2, HERC5, and CCL8 as prognostic candidates for breast cancer,” *Journal of Cellular Physiology*, vol. 235, no. 1, pp. 394–407, 2020.
- [95] G. Chen, M. Yu, J. Cao, H. Zhao, Y. Dai, Y. Cong, and G. Qiao, “Identification of candidate biomarkers correlated with poor prognosis of breast cancer based on bioinformatics analysis,” *Bioengineered*, vol. 12, no. 1, pp. 5149–5161, 1 2021.
- [96] C. C. Sun, S. J. Li, W. Hu, J. Zhang, Q. Zhou, C. Liu, L. L. Li, Y. Y. Songyang, F. Zhang, Z. L. Chen, G. Li, Z. Y. Bi, F. Y. Gong, T. Bo, Z. P. Yuan, W. D. Hu, B. T. Zhan, Q. Zhang, Q. Q. He, and D. J. Li, “Comprehensive analysis of the expression and prognosis for E2Fs in human breast cancer,” *Molecular Therapy*, vol. 27, no. 6, pp. 1153–1165, 6 2019.
- [97] M. Oshi, H. Takahashi, Y. Tokumaru, Y. Li, O. M. Rashid, R. Matsuyama, I. Endo, and K. Takabe, “G2M cell cycle pathway score as a prognostic biomarker of metastasis in estrogen receptor (ER)-positive breast cancer,” *International Journal of Molecular Sciences*, vol. 21, no. 8, p. 2921, 2020.
- [98] P. Wolter, S. Hanselmann, G. Pattschull, E. Schruf, and S. Gaubatz, “Central spindle proteins and mitotic kinesins are direct transcriptional targets of MuvB, B-MYB and FOXM1 in breast cancer cell lines and are potential targets for therapy,” *Oncotarget*, vol. 8, no. 7, pp. 11 160–11 172, 1 2017.
- [99] M. Ogino, T. Fujii, Y. Nakazawa, T. Higuchi, Y. Koibuchi, T. Oyama, J. Horiguchi, and K. Shirabe, “Implications of topoisomerase (TOP1 and TOP2 α) expression in patients with breast cancer,” *In Vivo*, vol. 34, no. 6, pp. 3483–3487, 11 2020.
- [100] J. Li, P. Sun, T. Huang, S. He, L. Li, and G. Xue, “Individualized chemotherapy guided by the expression of ERCC1, RRM1, TUBB3, TYMS and TOP2A genes versus classic chemotherapy in the treatment of breast cancer: A comparative effectiveness study,” *Oncology Letters*, vol. 21, no. 1, p. 21, 1 2021.
- [101] B. Seto, “Rapamycin and mTOR: a serendipitous discovery and implications for breast cancer,” *Clinical and Translational Medicine*, vol. 1, no. 1, p. e29, 2012.
- [102] Z. Qiu, Y. Li, B. Zeng, X. Guan, and H. Li, “Downregulated CDKN1C/p57kip2 drives tumorigenesis and associates with poor overall survival in breast cancer,” *Biochemical and Biophysical Research Communications*, vol. 497, no. 1, pp. 187–193, 2 2018.
- [103] T. Takeshita, M. Asaoka, E. Katsuta, S. J. Photiadis, S. Narayanan, L. Yan, and K. Takabe, “High expression of polo-like kinase 1 is associated with TP53 inactivation, DNA repair deficiency, and worse prognosis in ER positive Her2 negative breast cancer,” *American Journal of Translational Research*, vol. 11, no. 10, pp. 6507–6521, 10 2019.
- [104] M. Wang, M. Dai, Y.-s. Wu, Z. Yi, Y. Li, and G. Ren, “Immunoglobulin superfamily member 10 is a novel prognostic biomarker for breast cancer,” *PeerJ*, vol. 8, p. e10128, 10 2020.
- [105] M. Cai, H. Li, R. Chen, and X. Zhou, “MRPL13 promotes tumor cell proliferation, migration and EMT process in breast cancer through the PI3K-AKT-mTOR pathway,” *Cancer Management and Research*, vol. 13, pp. 2009–2024, 2 2021.
- [106] D. N. Brown, I. Caffa, G. Cirmena, D. Piras, A. Garuti, M. Gallo, S. Alberti, A. Nencioni, A. Ballestrero, and G. Zoppoli, “Squalene epoxidase is a bona fide oncogene by amplification with clinical relevance in breast cancer,” *Scientific Reports*, vol. 6, no. 1, p. 19435, 1 2016.
- [107] N. I. Kim, M. H. Park, S.-S. Kweon, N. Cho, and J. S. Lee, “Squalene epoxidase expression is associated with breast tumor progression and with a poor prognosis in breast cancer,” *Oncology Letters*, vol. 21, no. 4, p. 259, 4 2021.
- [108] R Development Core Team, *R: A Language and Environment for Statistical Computing*, R Foundation for Statistical Computing, Vienna, Austria, 2018. [Online]. Available: <http://www.R-project.org>
- [109] T. D. Downs, “Spherical regression,” *Biometrika*, vol. 90, no. 3, pp. 655–668, 2003.
- [110] T. W. Anderson, *An Introduction to multivariate statistical analysis*, ser. Wiley Series in Probability and Statistics. Wiley, 2003.

S1. SUPPLEMENT TO SECTION II

A. Derivation of the projected normal density function

Theorem S1. Suppose $\mathbf{Y} \sim \mathcal{N}_p(\boldsymbol{\mu}, \boldsymbol{\Sigma})$. with mean vector $\boldsymbol{\mu}$ and covariance matrix $\boldsymbol{\Sigma}$. Then, $\mathbf{X} = \mathbf{Y}/\|\mathbf{Y}\|$ follows a projected normal distribution $\mathcal{PN}_p(\boldsymbol{\mu}, \boldsymbol{\Sigma})$ and the density function of \mathbf{X} at $\mathbf{x} = \mathbf{y}/\|\mathbf{y}\|$ is given by,

$$f(\mathbf{x}; \boldsymbol{\mu}, \boldsymbol{\Sigma}) = (2\pi)^{-\frac{p}{2}} |\boldsymbol{\Sigma}|^{-\frac{1}{2}} \exp \left\{ -\frac{\boldsymbol{\mu}^\top \boldsymbol{\Sigma}^{-1} \boldsymbol{\mu}}{2} + \frac{m^2}{2v} \right\} \int_0^\infty R^{p-1} \exp \left\{ -\frac{1}{2v} (R - m)^2 \right\} dR, \quad (\text{S1})$$

where $R = \|\mathbf{y}\|$, $m = \mathbf{x}^\top \boldsymbol{\Sigma}^{-1} \boldsymbol{\mu} / \mathbf{x}^\top \boldsymbol{\Sigma}^{-1} \mathbf{x}$, $v = 1 / \mathbf{x}^\top \boldsymbol{\Sigma}^{-1} \mathbf{x}$.

Proof. Let $\mathbf{y} = (y_1, y_2, \dots, y_p)$ with $R = \|\mathbf{y}\|$, and $\mathbf{x} = (x_1, x_2, \dots, x_p) = \mathbf{y}/\|\mathbf{y}\|$ so that $\|\mathbf{x}\| = 1$. Define the representation of \mathbf{x} in the spherical coordinate system as $\boldsymbol{\theta} = (\theta_1, \theta_2, \dots, \theta_{p-1})$ so that

$$x_1 = \cos \theta_1; \quad x_j = \prod_{k=1}^{j-1} \sin \theta_k \cos \theta_j, \quad \text{for } j = 2, 3, \dots, p-1; \quad x_p = \prod_{k=1}^{p-1} \sin \theta_k, \quad (\text{S2})$$

with the Jacobian of transformation as $\mathbf{J}_x = \prod_{j=1}^{p-2} \sin^{(p-1-j)} \theta_j$. Then, we denote the transformation from $R, \boldsymbol{\theta}$ to \mathbf{y} as $\mathbf{y} = \mathbf{y}(R, \boldsymbol{\theta})$ which is given by,

$$y_1 = R \cos \theta_1; \quad y_j = R \prod_{k=1}^{j-1} \sin \theta_k \cos \theta_j, \text{ for } j = 2, 3, \dots, p-1; \quad y_p = R \prod_{k=1}^{p-1} \sin \theta_k, \quad (\text{S3})$$

with the Jacobian of transformation as $\mathbf{J}_y = R^{p-1} \prod_{j=1}^{p-2} \sin^{(p-1-j)} \theta_j$. Now, by the change of variables, the density function of $\boldsymbol{\theta}$ is given by,

$$f(\boldsymbol{\theta}; \boldsymbol{\mu}, \boldsymbol{\Sigma}) = \int_0^\infty \mathbf{J}_y (2\pi)^{-\frac{p}{2}} |\boldsymbol{\Sigma}|^{-\frac{1}{2}} \exp \left\{ -\frac{1}{2} (\mathbf{y}(R, \boldsymbol{\theta}) - \boldsymbol{\mu})^\top \boldsymbol{\Sigma}^{-1} (\mathbf{y}(R, \boldsymbol{\theta}) - \boldsymbol{\mu}) \right\} dR. \quad (\text{S4})$$

Then, by applying the change of variables again, the density function of \mathbf{x} is given by,

$$\begin{aligned} f(\mathbf{x}; \boldsymbol{\mu}, \boldsymbol{\Sigma}) &= \int_0^\infty \mathbf{J}_y / \mathbf{J}_x (2\pi)^{-\frac{p}{2}} |\boldsymbol{\Sigma}|^{-\frac{1}{2}} \exp \left\{ -\frac{1}{2} (R\mathbf{x} - \boldsymbol{\mu})^\top \boldsymbol{\Sigma}^{-1} (R\mathbf{x} - \boldsymbol{\mu}) \right\} dR \\ &= (2\pi)^{-\frac{p}{2}} |\boldsymbol{\Sigma}|^{-\frac{1}{2}} \exp \left\{ -\frac{\boldsymbol{\mu}^\top \boldsymbol{\Sigma}^{-1} \boldsymbol{\mu}}{2} + \frac{m^2}{2v} \right\} \int_0^\infty R^{p-1} \exp \left\{ -\frac{1}{2v} (R - m)^2 \right\} dR, \end{aligned} \quad (\text{S5})$$

where $m = \mathbf{x}^\top \boldsymbol{\Sigma}^{-1} \boldsymbol{\mu} / \mathbf{x}^\top \boldsymbol{\Sigma}^{-1} \mathbf{x}$, $v = 1 / \mathbf{x}^\top \boldsymbol{\Sigma}^{-1} \mathbf{x}$. □

B. Numerical computation of the MLE of $\boldsymbol{\mu}$

Theorem S2. Let \mathbf{B} be a $p \times p$ positive definite symmetric matrix, $\mathbf{b} \in \mathbb{R}^p$. Then, the unique global minimizer \mathbf{x}_0 that

$$\text{minimize } \text{Tr } \mathbf{B}^{-1} (\mathbf{b} - \mathbf{x})(\mathbf{b} - \mathbf{x})^\top \text{ subject to } \mathbf{x}^\top \mathbf{x} = 1 \quad (\text{S6})$$

is given by $\mathbf{x}_0 = (\mathbf{I} + \lambda_0 \mathbf{B})^{-1} \mathbf{b}$, where λ_0 lies between

- (1) $[0, \mathbf{b}^\top \mathbf{B}^{-1} \mathbf{b} / 2]$, if $\mathbf{b}^\top \mathbf{b} - 1 > 0$,
- (2) $\lambda = 0$, if $\mathbf{b}^\top \mathbf{b} - 1 = 0$,
- (3) $[(\mathbf{u}_m^\top \mathbf{b} / 2 - 1) / e_m, 0]$, if $\mathbf{b}^\top \mathbf{b} - 1 < 0$.

Where e_m , \mathbf{u}_m are the largest eigenvalue and corresponding eigenvector of \mathbf{B} .

Proof. The Lagrangian associated with (S6) is given by,

$$L(\mathbf{x}, \lambda) = \text{Tr } \mathbf{B}^{-1} (\mathbf{b} - \mathbf{x})(\mathbf{b} - \mathbf{x})^\top + \lambda (\mathbf{x}^\top \mathbf{x} - 1). \quad (\text{S7})$$

with a Lagrange multiplier λ . Setting $\nabla L = 0$ yields $\mathbf{x}_0 = (\mathbf{I} + \lambda \mathbf{B})^{-1} \mathbf{b}$ and $\mathbf{b}^\top (\mathbf{I} + \lambda \mathbf{B})^{-2} \mathbf{b} = 1$.

Let $f(\lambda) = \mathbf{b}^\top (\mathbf{I} + \lambda \mathbf{B})^{-2} \mathbf{b} - 1$, $\mathbf{B} = \mathbf{U} \mathbf{M} \mathbf{U}^\top$, $\mathbf{M} = \text{diag}\{e_j\}$, $j = 1, 2, \dots, p$ and $\mathbf{U}^\top \mathbf{b} = (c_1, c_2, \dots, c_p)^\top = \mathbf{c}$, then,

$$f(\lambda) = \mathbf{c}^\top (\mathbf{I} + \lambda \mathbf{M})^{-2} \mathbf{c} - 1 = \sum_{j=1}^p \frac{c_j^2}{(1 + \lambda e_j)^2} - 1$$

and

$$f'(\lambda) = -2 \sum_{j=1}^p \frac{c_j^2 e_j}{(1 + \lambda e_j)^3}, \quad f''(\lambda) = 6 \sum_{j=1}^p \frac{c_j^2 e_j^2}{(1 + \lambda e_j)^4}.$$

For $\lambda \geq 0$, $f(\lambda)$ is a continuous function with $f'(\lambda) < 0$ and

$$f(\lambda) = \sum_{j=1}^p \frac{c_j^2}{(1 + \lambda e_j)^2} - 1 \leq \sum_{j=1}^p \frac{c_j^2}{2\lambda e_j} - 1 = \frac{1}{2\lambda} \mathbf{b}^\top \mathbf{B}^{-1} \mathbf{b} - 1.$$

So,

$$\lambda > \frac{\mathbf{b}^\top \mathbf{B}^{-1} \mathbf{b}}{2} \Rightarrow f(\lambda) < 0$$

If $f(0) = \mathbf{b}^\top \mathbf{b} - 1 > 0$, we can then find the root of $f(\lambda) = 0$ in $[0, \mathbf{b}^\top \mathbf{B}^{-1} \mathbf{b} / 2]$.

If $\mathbf{b}^\top \mathbf{b} - 1 < 0$, no positive root exists. Then let $\lambda < 0$, we have

$$f(\lambda) = \sum_{j=1}^p \frac{c_j^2}{(1 + \lambda e_j)^2} - 1 \geq \frac{c_j^2}{(1 + \lambda e_j)^2} - 1.$$

For each $j = 1, 2, \dots, p$. So,

$$\frac{-\sqrt{c_j^2 - 1}}{e_j} < \lambda < \frac{\sqrt{c_j^2 - 1}}{e_j} \Rightarrow f(\lambda) > 0.$$

According to the Hessian matrix $\mathbf{H}_x = \mathbf{B}^{-1} + \lambda \mathbf{I}$, the unique global minimizer is obtained when $\lambda > -\frac{1}{e_m}$, where $e_m = \max\{e_1, e_2, \dots, e_p\}$. Let \mathbf{u}_m denote the corresponding eigenvector and $c_m = \mathbf{u}_m^\top \mathbf{b}$ in \mathbf{c} , then $-\frac{1}{e_j} \leq -\frac{1}{e_m} < \frac{0.5\sqrt{c_m^2 - 1}}{e_m}$, for $j = 1, 2, \dots, p$, and when $\lambda \geq \frac{0.5\sqrt{c_m^2 - 1}}{e_m}$, $f(\lambda)$ is continuous. Hence, we can find a negative root of $f(\lambda) = 0$ in $\left[\frac{0.5\sqrt{c_m^2 - 1}}{e_m}, 0\right]$. \square

C. Proof of Proposition 3

From Section II-B2, for fixed $\boldsymbol{\mu}_{t+1}$, Q_P is equivalent to

$$Q_P(\boldsymbol{\mu}_{t+1}, \boldsymbol{\Lambda}, \boldsymbol{\Psi}; \boldsymbol{\mu}_{t+1}, \boldsymbol{\Lambda}_t, \boldsymbol{\Psi}_t) = c - \frac{n}{2} \{\log \det(\boldsymbol{\Lambda} \boldsymbol{\Lambda}^\top + \boldsymbol{\Psi}) + \text{Tr}(\boldsymbol{\Lambda} \boldsymbol{\Lambda}^\top + \boldsymbol{\Psi})^{-1} \tilde{\mathbf{S}}_t\}, \quad (\text{S8})$$

where $\tilde{\mathbf{S}}_t = \frac{1}{n} \sum_{i=1}^n \mathbb{E}_{R_i | \mathbf{X}_i} \{(R_i \mathbf{X}_i - \boldsymbol{\mu}_{t+1})(R_i \mathbf{X}_i - \boldsymbol{\mu}_{t+1})^\top\}$.

From (S8), the ML estimators of $\boldsymbol{\Lambda}$ and $\boldsymbol{\Psi}$ are obtained by solving the score equations

$$\begin{cases} \boldsymbol{\Lambda}(\mathbf{I}_q + \boldsymbol{\Lambda}^\top \boldsymbol{\Psi}^{-1} \boldsymbol{\Lambda}) = \tilde{\mathbf{S}}_t \boldsymbol{\Psi}^{-1} \boldsymbol{\Lambda} \\ \boldsymbol{\Psi} = \text{diag}(\tilde{\mathbf{S}}_t - \boldsymbol{\Lambda} \boldsymbol{\Lambda}^\top) \end{cases} \quad (\text{S9})$$

From $\boldsymbol{\Lambda}(\mathbf{I}_q + \boldsymbol{\Lambda}^\top \boldsymbol{\Psi}^{-1} \boldsymbol{\Lambda}) = \tilde{\mathbf{S}}_t \boldsymbol{\Psi}^{-1} \boldsymbol{\Lambda}$, we have

$$\boldsymbol{\Psi}^{-1/2} \boldsymbol{\Lambda}(\mathbf{I}_q + (\boldsymbol{\Psi}^{-1/2} \boldsymbol{\Lambda})^\top \boldsymbol{\Psi}^{-1/2} \boldsymbol{\Lambda}) = \boldsymbol{\Psi}^{-1/2} \tilde{\mathbf{S}}_t \boldsymbol{\Psi}^{-1/2} \boldsymbol{\Psi}^{-1/2} \boldsymbol{\Lambda}. \quad (\text{S10})$$

Suppose that $\boldsymbol{\Psi}^{-1/2} \tilde{\mathbf{S}}_t \boldsymbol{\Psi}^{-1/2} = \mathbf{V} \mathbf{D} \mathbf{V}^\top$ and that the diagonal elements in \mathbf{D} are in decreasing order with $\theta_1 \geq \theta_2 \geq \dots \geq \theta_p$. Let $\mathbf{D} = \begin{bmatrix} \mathbf{D}_q & 0 \\ 0 & \mathbf{D}_m \end{bmatrix}$ with $m = p - q$ and \mathbf{D}_q containing the largest q eigenvalues $\theta_1 \geq \theta_2 \geq \dots \geq \theta_q$. The corresponding q eigenvectors form columns of the matrix \mathbf{V}_q so that $\mathbf{V} = [\mathbf{V}_q, \mathbf{V}_m]$. Then, if $\mathbf{D}_q > \mathbf{I}_q$, (S10) shows that

$$\boldsymbol{\Lambda} = \boldsymbol{\Psi}^{1/2} \mathbf{V}_q (\mathbf{D}_q - \mathbf{I}_q)^{1/2}. \quad (\text{S11})$$

Hence, conditional on $\boldsymbol{\Psi}$, $\boldsymbol{\Lambda}$ is maximized at $\hat{\boldsymbol{\Lambda}} = \boldsymbol{\Psi}^{1/2} \mathbf{V}_q \boldsymbol{\Delta}$, where $\boldsymbol{\Delta}$ is a diagonal matrix with elements $\max(\theta_i - 1, 0)^{1/2}$, $i = 1, \dots, q$.

From the construction of \mathbf{V}_q and \mathbf{V}_m , we have $\mathbf{V}_q^\top \mathbf{V}_q = \mathbf{I}_q$, $\mathbf{V}_m^\top \mathbf{V}_m = \mathbf{I}_m$, $\mathbf{V}_q \mathbf{V}_q^\top + \mathbf{V}_m \mathbf{V}_m^\top = \mathbf{I}_p$, $\mathbf{V}_q^\top \mathbf{V}_m = \mathbf{0}$ and hence, $(\mathbf{V}_q \mathbf{D}_q \mathbf{V}_q^\top + \mathbf{V}_m \mathbf{V}_m^\top)(\mathbf{V}_q \mathbf{D}_q^{-1} \mathbf{V}_q^\top + \mathbf{V}_m \mathbf{V}_m^\top) = \mathbf{I}_p$.

Let $\mathbf{A} = \mathbf{V}_q \boldsymbol{\Delta}^2 \mathbf{V}_q^\top$. Then $\mathbf{A} \mathbf{A} = \mathbf{V}_q \boldsymbol{\Delta}^4 \mathbf{V}_q^\top$ and

$$\begin{aligned} |\mathbf{A} + \mathbf{I}_p| &= |(\mathbf{A} + \mathbf{I}_p) \mathbf{A}| / |\mathbf{A}| \\ &= |\mathbf{V}_q (\boldsymbol{\Delta}^4 + \boldsymbol{\Delta}^2) \mathbf{V}_q^\top| / |\mathbf{V}_q \boldsymbol{\Delta}^2 \mathbf{V}_q^\top| \\ &= |\boldsymbol{\Delta}^2 + \mathbf{I}_q| = \prod_{j=1}^q \theta_j \end{aligned} \quad (\text{S12})$$

and

$$\begin{aligned} (\mathbf{A} + \mathbf{I}_p)^{-1} &= (\mathbf{V}_q \boldsymbol{\Delta}^2 \mathbf{V}_q^\top + \mathbf{V}_q \mathbf{V}_q^\top + \mathbf{V}_m \mathbf{V}_m^\top)^{-1} \\ &= (\mathbf{V}_q (\boldsymbol{\Delta}^2 + \mathbf{I}_q) \mathbf{V}_q^\top + \mathbf{V}_m \mathbf{V}_m^\top)^{-1} \\ &= (\mathbf{V}_q \mathbf{D}_q \mathbf{V}_q^\top + \mathbf{V}_m \mathbf{V}_m^\top)^{-1} \\ &= \mathbf{V}_q \mathbf{D}_q^{-1} \mathbf{V}_q^\top + \mathbf{V}_m \mathbf{V}_m^\top. \end{aligned} \quad (\text{S13})$$

Based on (S12) and (S13) and (9), the profile log-likelihood is given by,

$$\begin{aligned}
Q_p(\Psi) &= c' - \frac{n}{2} \log |\hat{\Lambda} \hat{\Lambda}^\top + \Psi| - \frac{n}{2} \text{Tr} (\hat{\Lambda} \hat{\Lambda}^\top + \Psi)^{-1} \tilde{\mathbf{S}}_t \\
&= c' - \frac{n}{2} \left\{ \log |\Psi^{1/2} (\mathbf{V}_q \Delta^2 \mathbf{V}_q^\top + \mathbf{I}_p) \Psi^{1/2}| + \text{Tr} (\Psi^{1/2} (\mathbf{V}_q \Delta^2 \mathbf{V}_q^\top + \mathbf{I}_p) \Psi^{1/2})^{-1} \tilde{\mathbf{S}}_t \right\} \\
&= c' - \frac{n}{2} \left\{ \log \det \Psi + \log |\mathbf{V}_q \Delta^2 \mathbf{V}_q^\top + \mathbf{I}_p| + \text{Tr} (\mathbf{V}_q \mathbf{D}_q^{-1} \mathbf{V}_q^\top + \mathbf{V}_m \mathbf{V}_m^\top) \Psi^{-1/2} \tilde{\mathbf{S}}_t \Psi^{-1/2} \right\} \\
&= c' - \frac{n}{2} \left\{ \log \det \Psi + \sum_{j=1}^q \log \theta_j + \text{Tr} \mathbf{D}_q^{-1} \mathbf{V}_q^\top \mathbf{V} \mathbf{D} \mathbf{V}^\top \mathbf{V}_q + \text{Tr} \mathbf{V}_m^\top \mathbf{V} \mathbf{D} \mathbf{V}^\top \mathbf{V}_m \right\} \\
&= c' - \frac{n}{2} \left\{ \log \det \Psi + \sum_{j=1}^q \log \theta_j + \text{Tr} \mathbf{D}_q^{-1} \mathbf{D}_q + \text{Tr} \mathbf{D}_m \right\} \\
&= c' - \frac{n}{2} \left\{ \log \det \Psi + \sum_{j=1}^q \log \theta_j + q + \text{Tr} \Psi^{-1} \tilde{\mathbf{S}}_t - \sum_{j=1}^q \theta_j \right\},
\end{aligned} \tag{S14}$$

where c' is a constant that does not depend on Ψ .

D. Recursive formulas

Let $\mathcal{I}_k = \int_0^\infty R^k \exp \left\{ -\frac{1}{2v} (R - m)^2 \right\} dR$ with $m \in \mathbb{R}$, $v > 0$, $k \in \mathbb{N}$, then,

$$\begin{aligned}
\mathcal{I}_k &= \frac{R^{k+1}}{k+1} \exp \left\{ -\frac{1}{2v} (R - m)^2 \right\} \Big|_0^\infty - \int_0^\infty \frac{R^{k+1}}{k+1} \exp \left\{ -\frac{1}{2v} (R - m)^2 \right\} \left(-\frac{R}{v} + \frac{m}{v} \right) dR \\
&= \frac{1}{v(k+1)} \mathcal{I}_{k+2} - \frac{m}{v(k+1)} \mathcal{I}_{k+1}.
\end{aligned}$$

That is, $\mathcal{I}_{k+2} = m \mathcal{I}_{k+1} + (k+1)v \mathcal{I}_k$. Then, $\frac{\mathcal{I}_{k+2}}{\mathcal{I}_{k+1}} = m + (k+1)v \frac{\mathcal{I}_k}{\mathcal{I}_{k+1}}$, $\frac{\mathcal{I}_{k+2}}{\mathcal{I}_k} = (k+1)v + m \frac{\mathcal{I}_{k+1}}{\mathcal{I}_k}$.

E. FADS-D: E- and CM-step computation

The conditional expectations of \mathbf{Z}_i , $\mathbf{Z}_i \mathbf{Z}_i^\top$ and R_i , \mathbf{Z}_i given \mathbf{X} are

$$\begin{aligned}
\mathbb{E}_{\mathbf{Z}_i | \mathbf{X}_i}(\mathbf{Z}_i) &= \mathbb{E}_{R_i | \mathbf{X}_i} \{ \mathbb{E}_{\mathbf{Z}_i | R_i, \mathbf{X}_i}(\mathbf{Z}_i) \}, \quad \mathbb{E}_{\mathbf{Z}_i | \mathbf{X}_i}(\mathbf{Z}_i \mathbf{Z}_i^\top) = \mathbb{E}_{R_i | \mathbf{X}_i} \{ \mathbb{E}_{\mathbf{Z}_i | R_i, \mathbf{X}_i}(\mathbf{Z}_i \mathbf{Z}_i^\top) \}, \\
\mathbb{E}_{\mathbf{Z}_i, R_i | \mathbf{X}_i}(R_i \mathbf{Z}_i^\top) &= \mathbb{E}_{R_i | \mathbf{X}_i} \{ R_i \mathbb{E}_{\mathbf{Z}_i | R_i, \mathbf{X}_i}(\mathbf{Z}_i^\top) \}.
\end{aligned}$$

The joint density function of R_i , \mathbf{X}_i , \mathbf{Z}_i is given by,

$$\begin{aligned}
f_{r,x,z}(R_i, \mathbf{X}_i, \mathbf{Z}_i) &= f_{y|z}(\mathbf{Y}_i | \mathbf{Z}_i) |\mathbf{J}_i| \cdot f_z(\mathbf{Z}_i) \\
&\propto \exp \left\{ -\frac{1}{2} (R_i \mathbf{X}_i - \boldsymbol{\mu} - \boldsymbol{\Lambda} \mathbf{Z}_i)^\top \Psi^{-1} (R_i \mathbf{X}_i - \boldsymbol{\mu} - \boldsymbol{\Lambda} \mathbf{Z}_i) - \frac{1}{2} \mathbf{Z}_i^\top \mathbf{Z}_i \right\}.
\end{aligned} \tag{S15}$$

Then, by the conditional normal distribution, we have

$$\begin{aligned}
\mathbb{E}_{\mathbf{Z}_i | \mathbf{X}_i}(\mathbf{Z}_i) &= \boldsymbol{\Lambda}^\top \boldsymbol{\Sigma}^{-1} \{ \mathbb{E}_{R_i | \mathbf{X}_i}(R_i) \mathbf{X}_i - \boldsymbol{\mu} \}, \\
\mathbb{E}_{\mathbf{Z}_i, R_i | \mathbf{X}_i}(R_i \mathbf{Z}_i^\top) &= \{ \mathbb{E}_{R_i | \mathbf{X}_i}(R_i^2) \mathbf{X}_i^\top - \mathbb{E}_{R_i | \mathbf{X}_i}(R_i) \boldsymbol{\mu}^\top \} \boldsymbol{\Sigma}^{-1} \boldsymbol{\Lambda}, \\
\mathbb{E}_{\mathbf{Z}_i | \mathbf{X}_i}(\mathbf{Z}_i \mathbf{Z}_i^\top) &= (\mathbf{I} + \boldsymbol{\Lambda}^\top \Psi^{-1} \boldsymbol{\Lambda})^{-1} + \boldsymbol{\Lambda}^\top \boldsymbol{\Sigma}^{-1} \{ \mathbb{E}_{R_i | \mathbf{X}_i}(R_i^2) \mathbf{X}_i \mathbf{X}_i^\top - \mathbb{E}_{R_i | \mathbf{X}_i}(R_i) (\boldsymbol{\mu} \mathbf{X}_i^\top + \mathbf{X}_i \boldsymbol{\mu}^\top) + \boldsymbol{\mu} \boldsymbol{\mu}^\top \} \boldsymbol{\Sigma}^{-1} \boldsymbol{\Lambda}.
\end{aligned}$$

Then, conditional on $\hat{\boldsymbol{\mu}}_{t+1}$ and Ψ_t , the CM-step for $\boldsymbol{\Lambda}_{t+1}$ is given by,

$$\hat{\boldsymbol{\Lambda}}_{t+1} = \left\{ \sum_{i=1}^n \mathbf{X}_i \mathbb{E}_{\mathbf{Z}_i, R_i | \mathbf{X}_i}(R_i \mathbf{Z}_i^\top) - \hat{\boldsymbol{\mu}}_{t+1} \sum_{i=1}^n \mathbb{E}_{\mathbf{Z}_i | \mathbf{X}_i}(\mathbf{Z}_i^\top) \right\} \left\{ \sum_{i=1}^n \mathbb{E}_{\mathbf{Z}_i | \mathbf{X}_i}(\mathbf{Z}_i \mathbf{Z}_i^\top) \right\}^{-1}. \tag{S16}$$

Conditional on $\hat{\boldsymbol{\mu}}_{t+1}$ and $\hat{\boldsymbol{\Lambda}}_{t+1}$, the CM-step for Ψ_{t+1} is given by,

$$\begin{aligned}
\hat{\Psi}_{t+1} &= \frac{1}{n} \text{diag} \left\{ \sum_{i=1}^n \mathbb{E}_{R_i | \mathbf{X}_i}(R_i^2) \mathbf{X}_i \mathbf{X}_i^\top - 2 \hat{\boldsymbol{\mu}}_{t+1} \sum_{i=1}^n \mathbb{E}_{R_i | \mathbf{X}_i}(R_i) \mathbf{X}_i^\top \right. \\
&\quad - 2 \hat{\boldsymbol{\Lambda}}_{t+1} \sum_{i=1}^n \mathbb{E}_{\mathbf{Z}_i, R_i | \mathbf{X}_i}(R_i \mathbf{Z}_i) \mathbf{X}_i^\top + 2 \hat{\boldsymbol{\mu}}_{t+1} \sum_{i=1}^n \mathbb{E}_{\mathbf{Z}_i | \mathbf{X}_i}(\mathbf{Z}_i^\top) \hat{\boldsymbol{\Lambda}}_{t+1}^\top \\
&\quad \left. + \hat{\boldsymbol{\Lambda}}_{t+1} \sum_{i=1}^n \mathbb{E}_{\mathbf{Z}_i | \mathbf{X}_i}(\mathbf{Z}_i \mathbf{Z}_i^\top) \hat{\boldsymbol{\Lambda}}_{t+1}^\top + n \hat{\boldsymbol{\mu}}_{t+1} \hat{\boldsymbol{\mu}}_{t+1}^\top \right\}.
\end{aligned} \tag{S17}$$

The non-positive values in $\hat{\Psi}_{t+1}$ are truncated to a small positive number [110].

S2. SUPPLEMENT TO SECTION III

A. Average iterations and convergence rates

TABLE S1: Average iterations (in converged cases for both FADS-P and FADS-D) and convergence rates (in %) of FADS-P and FADS-D algorithms applied to randomly simulated datasets where true $(n, p, q) = (300, 30, 3)$.

		1	2	3	4	5	6
FADS-P	iteration	109	67	48	83	107	115
	convergence rate	100	100	100	100	100	100
FADS-D	iteration	257	341	595	885	1438	2732
	convergence rate	100	100	100	92	82	70

TABLE S2: Average iterations (in converged cases for both FADS-P and FADS-D) and convergence rates (in %) of FADS-P and FADS-D algorithms applied to randomly simulated datasets where true $(n, p, q) = (300, 30, 5)$.

		1	2	3	4	5	6	7	8	9	10
FADS-P	iteration	127	88	70	62	33	76	89	102	111	147
	convergence rate	100	100	100	100	100	100	100	100	100	100
FADS-D	iteration	378	467	570	820	1304	1952	2312	3225	3296	4091
	convergence rate	91	94	98	100	100	82	55	38	28	24

TABLE S3: Average iterations (in converged cases for both FADS-P and FADS-D) and convergence rates (in %) of FADS-P and FADS-D algorithms applied to randomly simulated datasets where true $(n, p, q) = (1000, 100, 3)$.

		1	2	3	4	5	6
FADS-P	iteration	683	208	123	141	275	402
	convergence rate	100	100	100	100	100	100
FADS-D	iteration	1411	2075	3156	3120	3864	4042
	convergence rate	100	100	100	100	100	100

TABLE S4: Average iterations (in converged cases for both FADS-P and FADS-D) and convergence rates (in %) of FADS-P and FADS-D algorithms applied to randomly simulated datasets where true $(n, p, q) = (1000, 100, 5)$.

		1	2	3	4	5	6	7	8	9	10
FADS-P	iteration	789	231	275	233	141	204	307	456	475	601
	convergence rate	100	100	100	100	100	100	100	100	100	100
FADS-D	iteration	2281	2411	3581	4498	5818	6185	6971	7269	7206	7189
	convergence rate	100	100	100	100	96	79	72	65	64	59

B. Average CPU time

TABLE S5: Average CPU time (in seconds) of FADS-P and FADS-D algorithms applied to randomly simulated datasets (Converged cases).

		1	2	3	4	5	6	7	8	9	10
$(n, p, q) = (300, 30, 3)$	FADS-P	7.570	5.640	3.451	6.826	9.241	10.239	-	-	-	-
	FADS-D	10.411	13.965	24.603	36.619	59.461	113.415	-	-	-	-
$(n, p, q) = (300, 30, 5)$	FADS-P	7.983	6.248	5.901	4.594	2.171	5.698	7.014	8.718	10.044	13.119
	FADS-D	15.229	18.929	23.348	33.641	54.090	81.192	97.207	134.969	138.628	168.619
$(n, p, q) = (1000, 100, 3)$	FADS-P	134.633	47.134	26.230	36.970	76.216	111.779	-	-	-	-
	FADS-D	219.185	331.254	503.038	498.516	620.895	644.078	-	-	-	-
$(n, p, q) = (1000, 100, 5)$	FADS-P	145.243	46.902	60.470	49.188	27.735	49.616	78.007	121.077	131.134	172.879
	FADS-D	354.947	381.501	570.623	710.967	927.920	1007.009	1147.169	1189.592	1184.188	1178.299

C. Data-driven cases: Relative Frobenius distances of FADS-P estimates

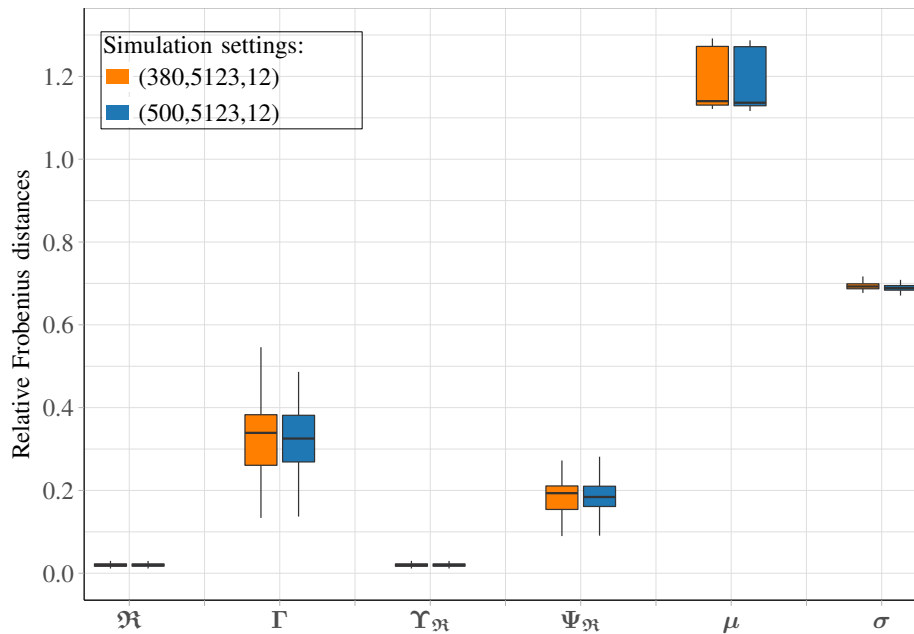


Fig. S1: Data-driven cases: Relative Frobenius distances of FADS-P for \mathfrak{R} , Γ , $\Upsilon_{\mathfrak{R}}$, $\Psi_{\mathfrak{R}}$, σ and μ .

S3. SUPPLEMENT TO SECTION IV

A. List of words in #MeToo tweets

Figures S2–S5 together present the 721 words (in alphabetical order along columns) for the final data matrix of the #MeToo tweet data that were collected and analyzed in Section IV-A.

abc	cbs	drop	harass	marchforourlives	process	smear	wave
absolute	cbsnews	due	hard	mark	produce	snowflake	wear
abuse	celeb	dumb	harm	market	professional	social	week
accept	ceo	dunham	hart	marry	professor	society	weinstein
account	challenge	easy	hat	matter	progress	solute	white
accuse	chance	economy	hate	media	project	son	wife
act	change	educate	head	meet	proof	song	win
activism	charge	effect	heal	mental	protect	sound	witchhunt
actor	check	elect	hear	mention	protest	space	women
actress	child	employ	hearmetoo	mentoo	proud	speak	womenmarch
actual	china	employee	heart	mentor	prove	special	word
add	choice	employer	hill	message	public	speech	worker
address	church	empower	hillary	mgtow	publish	staff	workplace
admit	churchtoo	encourage	hire	michaeljackson	pull	stand	world
adopt	claim	enjoy	history	milano	punish	standard	worry
advance	class	entertain	hit	millennials	push	star	worse
advice	classic	entire	hold	mind	qanon	start	worth
advocate	clean	environment	holiday	misconduct	question	stay	writ
affect	cleveland	episode	hollywood	misogyny	quiet	step	write
afraid	climate	epstein	home	miss	quote	stop	wrong
against	clinton	equal	honor	mjakabar	racism	store	youtube
age	close	era	hope	model	radio	story	
agenda	club	event	horror	mom	raise	strategy	
agree	cnn	evidence	host	moment	rape	street	
aide	cold	evil	house	money	rapist	strong	
air	colleague	excuse	huge	month	reach	struggle	
allege	college	exist	human	moonves	read	student	
amaze	comment	expect	hurt	moral	real	stuff	
anger	commit	experience	husband	morn	reality	stupid	
answer	common	explain	hypocrisy	mote	realize	subject	

Fig. S2: Word list for #MeToo tweet data, part 1

antifa	community	exploit	idea	move	reason	sue
anymore	company	expose	idiot	movement	receive	suffer
apology	compassion	extreme	ignore	movie	recent	suggest
apparent	complain	eye	illegal	msnbc	relate	suit
apply	complete	facebook	imagine	mueller	religion	support
argue	concern	fail	impact	murder	remain	suppose
arrest	congress	fair	inappropriate	music	republic	surprise
art	consequence	fake	include	nation	republican	survey
article	conservative	fall	india	neiltyson	resign	survive
assault	continue	false	indigenous	newyork	resist	suspend
attack	control	family	individual	nfl	resistance	system
attempt	controversy	fan	industry	nice	respect	tact
attention	conversation	farm	info	night	response	taking
attitude	convict	fbi	innocent	note	responsible	talk
attorney	cord	fear	inspire	nyt	result	taranaburke
australia	corporate	feel	interview	obama	reveal	target
avenatti	correct	female	investigate	ocasio	rich	taxpayer
avoid	corrupt	feminism	involve	offend	ridiculous	teach
award	cosby	fend	issue	offensive	right	team
aware	cost	fight	jail	officer	rise	teen
baby	count	figure	job	official	risk	tell
backfire	country	file	joebiden	opine	role	term
backlash	courage	final	join	opportunity	ruin	text
bad	court	finance	joke	organize	rule	thehill
ban	cover	fine	journalism	origin	run	theview
base	crap	fire	judge	oscars	sad	thread
basic	crazy	fit	jump	outrage	safe	threat
bate	create	fix	justice	panel	santa	time
baylor	credit	flight	kamalaharris	parent	save	timesup
beat	creep	flirt	kavanaugh	partner	scandal	tire

Fig. S3: Word list for #MeToo tweet data, part 2

beauty	crime	focus	kick	party	scar	top
begin	crisis	folk	kid	pass	school	topic
behave	cry	follow	kill	passe	science	total
believe	culture	force	kiss	past	scream	touch
bias	current	ford	lack	patriarchy	search	toxic
big	dad	forget	lady	pay	season	train
bit	daily	form	laugh	pedophile	secret	trauma
black	damage	forward	law	pence	seek	treat
blacklivesmatter	date	found	lawsuit	people	segregate	trend
blame	daughter	founder	lawyer	perfect	sell	trial
blexit	day	fox	lead	perpetrator	senator	trouble
block	daysofactivism	france	learn	person	send	trump
blog	deal	free	lease	personal	senior	trust
bloomberg	death	friend	leave	photo	sense	truth
bluewave	decade	front	left	physical	sentence	tv
board	decent	fun	leftist	pic	series	type
body	decision	fund	legal	pick	serve	tyson
book	deep	funny	level	piece	service	un aids
boss	defense	fuse	lgbt	plan	set	understand
boy	demand	future	lgbtq	platform	settle	unintend
boycott	democrat	gain	liberal	play	settlement	university
brave	deny	game	lie	playlist	sex	usa
break	dependent	gay	life	podcast	sexism	verse
brexit	destroy	gender	light	police	sexual	veteran
bring	die	generate	line	policy	shame	victim
brown	difference	girl	link	poor	share	video
build	difficult	glad	list	port	shock	view
bully	dinner	global	listen	position	shoot	vinoddua
bunch	direct	govern	literal	post	short	violate
bush	director	government	live	potential	shut	violence
busy	discriminate	grope	lose	power	sick	virgin

Fig. S4: Word list for #MeToo tweet data, part 3

busy	discriminate	grope	lose	power	sick	virgin
buy	discussion	grow	love	powerful	silence	voice
california	diversity	guess	low	practice	simple	vote
call	dnc	guilt	lyric	predator	sing	wait
campaign	domestic	gun	mad	president	single	wake
canada	door	gust	maddock	press	sister	walk
car	doubt	hand	maga	prevent	sit	wall
care	dress	handle	major	prison	situation	war
career	drink	happen	male	private	sleep	washingtonpost
caught	drive	happy	manage	privilege	smart	watch

Fig. S5: Word list for #MeToo tweet data, part 4

B. Handwritten digits



Fig. S6: (a) Original and (b) Jittered images of 20 handwritten digits. The two sets are essentially indistinguishable.